

Quasiparticle Interfacial Level Alignment of Highly Hybridized Frontier Levels: H₂O on TiO₂(110)

Annapaola Migani,^{*,†,‡} Duncan J. Mowbray,[¶] Jin Zhao,^{§,||} and Hrvoje Petek[⊥]

[†]ICN2 - Institut Català de Nanociència i Nanotecnologia, ICN2 Building, Campus UAB, E-08193 Bellaterra, Barcelona, Spain

[‡]CSIC - Consejo Superior de Investigaciones Científicas, ICN2 Building, Campus UAB, E-08193 Bellaterra, Barcelona, Spain

[¶]Nano-Bio Spectroscopy Group and ETSF Scientific Development Center, Departamento de Física de Materiales, Universidad del País Vasco UPV/EHU and DIPC, E-20018 San Sebastián, Gipuzkoa, Spain

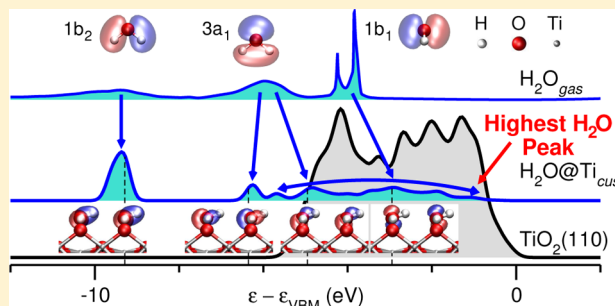
[§]Department of Physics and ICQD/HFNL, University of Science and Technology of China, Hefei, Anhui 230026, China

^{||}Synergetic Innovation Center of Quantum Information & Quantum Physics, University of Science and Technology of China, Hefei, Anhui 230026, China

[⊥]Department of Physics and Astronomy, University of Pittsburgh, Pittsburgh, Pennsylvania 15260, United States

Supporting Information

ABSTRACT: Knowledge of the frontier levels' alignment prior to photoirradiation is necessary to achieve a complete quantitative description of H₂O photocatalysis on TiO₂(110). Although H₂O on rutile TiO₂(110) has been thoroughly studied both experimentally and theoretically, a quantitative value for the energy of the highest H₂O occupied levels is still lacking. For experiment, this is due to the H₂O levels being obscured by hybridization with TiO₂(110) levels in the difference spectra obtained via ultraviolet photoemission spectroscopy (UPS). For theory, this is due to inherent difficulties in properly describing many-body effects at the H₂O–TiO₂(110) interface. Using the projected density of states (DOS) from state-of-the-art quasiparticle (QP) G_0W_0 , we disentangle the adsorbate and surface contributions to the complex UPS spectra of H₂O on TiO₂(110). We perform this separation as a function of H₂O coverage and dissociation on stoichiometric and reduced surfaces. Due to hybridization with the TiO₂(110) surface, the H₂O 3a₁ and 1b₁ levels are broadened into several peaks between 5 and 1 eV below the TiO₂(110) valence band maximum (VBM). These peaks have both intermolecular and interfacial bonding and antibonding character. We find the highest occupied levels of H₂O adsorbed intact and dissociated on stoichiometric TiO₂(110) are 1.1 and 0.9 eV below the VBM. We also find a similar energy of 1.1 eV for the highest occupied levels of H₂O when adsorbed dissociatively on a bridging O vacancy of the reduced surface. In both cases, these energies are significantly higher (by 0.6 to 2.6 eV) than those estimated from UPS difference spectra, which are inconclusive in this energy region. Finally, we apply self-consistent QPGW (scQPGW1) to obtain the ionization potential of the H₂O–TiO₂(110) interface.



1. INTRODUCTION

The photooxidation activity of a surface is determined by the interfacial level alignment between the occupied adsorbate levels and those of the substrate.^{1,2} Water photooxidation on TiO₂ has attracted enormous attention^{3–10} for energy applications^{11,12} based on H₂ production.¹³ This reaction also plays an important role in photocatalytic environmental remediation and surface self-cleaning/sterilizing.^{1,2,14} This is because the resulting hydroxyl radicals are the key intermediates in the oxidative degradation of organic species.^{15,16} To understand water photooxidation, it is necessary to understand the interfacial level alignment between the occupied levels of H₂O and the TiO₂ substrate.¹⁷

Experimentally, the most common approach to access the adsorbate levels is to take the difference between the covered and clean surface spectra from photoemission spectroscopy. However, when the adsorbate and surface levels are strongly hybridized, it becomes difficult to disentangle the adsorbate and surface contributions to the UPS spectra using only the difference spectra.¹⁸ For example, shifting of the surface levels due to hybridization or band bending may completely obscure the adsorbate levels.¹⁸ Further, the adsorbate levels near the valence band maximum (VBM) are the most likely to be obscured. It is precisely these levels that are most important for

Received: August 27, 2014

Published: November 21, 2014



photooxidation processes. Using a theoretical approach, one can directly disentangle the molecular levels by projecting the density of states (DOS) of the interface onto the atomic orbitals of the molecule. Altogether, this makes a robust theoretical approach necessary to accurately predict the alignment of the adsorbate and substrate levels, and separate the adsorbate and surface spectra.

A robust theoretical treatment requires quasiparticle (QP) G_0W_0 to capture the anisotropic screening of the electron–electron interaction at the interface.^{19–21} As previously demonstrated for CH₃OH on TiO₂(110), QP G_0W_0 is necessary to obtain even a qualitative description of the level alignment.^{22–24} For this interface, the occupied levels of the molecule are only weakly hybridized with the surface levels. This allowed an unambiguous comparison to the photoemission difference spectrum.²² However, for H₂O on rutile TiO₂(110), this is not the case.

The occupied molecular levels of H₂O on single crystal rutile TiO₂(110) have been probed via ultraviolet photoemission spectroscopy (UPS)^{18,25,26} and metastable impact electron spectroscopy (MIES).²⁶ These experiments were performed under ultrahigh vacuum (UHV) conditions from low to room temperature,²⁵ from 0.01 to 100 L H₂O exposure,¹⁸ and for various surface preparations resulting in either reduced TiO_{2-x}(110) with surface oxygen defects or “nearly-perfect” TiO₂(110).¹⁸ Altogether, these experiments have addressed the long-standing controversy as to where and how H₂O adsorbs and dissociates on TiO₂(110).^{27–36}

At 150 K the photoemission difference spectrum between H₂O covered and clean TiO₂(110) surfaces consists of three peaks, which are attributed to intact H₂O adsorbed on Ti coordinately unsaturated sites (Ti_{cus}).²⁵ Upon heating to 300 K, the difference spectrum’s three-peak structure evolves into a two-peak structure, which is attributed to dissociated H₂O adsorbed on bridging O vacancies (O_{br}^{vac}), i.e., O_{br}H surface species.²⁵ This assignment of the UPS spectra to intact (I) H₂O@Ti_{cus} or dissociated (D) H₂O@O_{br}^{vac} is based on the peak energy separations being consistent with those reported for H₂O³⁷ in gas phase or OH[−] in NaOH.³⁸

A comparison to the H₂O and OH[−] peaks is robust for the molecular levels that lie below and have little hybridization with the surface DOS. However, the adsorbate levels that lie within the surface valence band may significantly hybridize with the surface, with a single molecular level contributing to many interfacial levels. These interfacial levels are thus not easily associated with H₂O and OH[−] levels. This is exacerbated by the mixing of the molecular levels due to symmetry breaking at the interface. As a result, “between 5 and 8 eV” below the Fermi level, experimentally they “are unable to produce reliable difference structures” from the UPS spectra obtained for “nearly-perfect” TiO₂(110) exposed to H₂O at 160 K.¹⁸

Using the QP G_0W_0 H₂O projected DOS (PDOS), we have disentangled the adsorbate and surface contributions to the UPS spectra within this difficult energy range. This has been done as a function of H₂O coverage and dissociation on stoichiometric and reduced surfaces. In so doing, we provide quantitative values for the energies of the highest H₂O occupied levels, prior to photoirradiation, for a number of experimentally relevant^{3,5–7,15} H₂O–TiO₂(110) structures.

To directly compare to red-ox potentials, the important quantities for determining photoelectrocatalytic activity, one needs the alignment relative to the vacuum level, E_{vac} .^{39,40} With this, one obtains the ionization potential directly from $-\epsilon_{peak}^{PDOS} +$

E_{vac} . To obtain a more accurate absolute level alignment, we employ our recently introduced self-consistent QP GW^{41–43} technique scQPGW1.²²

The presentation of the results is organized as follows. First, we focus on the H₂O levels that lie below and have little hybridization with the substrate DOS. This is done for intact H₂O@Ti_{cus} in Section 3.1 and dissociated H₂O@O_{br}^{vac} in Section 3.2. Further, in Section 3.3, we show that these results are rather independent of the choice of xc-functional. In so doing we provide evidence for a robust semiquantitative agreement with the UPS difference spectra for the adsorbate levels for which an unambiguous comparison with the experiment is possible. For a more complete understanding of the UPS experiments, in Section 3.4 we analyze the H₂O PDOS for a variety of other H₂O structures on the stoichiometric and reduced surfaces. These may form under different experimental conditions and surface preparations. In Section 3.5 we focus on the highest H₂O occupied levels, which are significantly hybridized with the substrate DOS. The success of the QP G_0W_0 PDOS strategy for the lower-energy part of the UPS difference spectra provides support for our results in this difficult spectral region, where a straightforward comparison with experiment is not possible. Finally, in Section 3.6, we employ scQPGW1 to obtain an improved absolute level alignment relative to E_{vac} and thus estimate the ionization potential of the H₂O–TiO₂(110) interface.

2. METHODOLOGY

Our QP G_0W_0 calculations^{44–46} have been performed using vasp within the projector augmented wave (PAW) scheme.⁴⁷ The G_0W_0 calculations are based on Kohn–Sham wave functions and eigenenergies from density functional theory (DFT) obtained using a generalized gradient approximation (PBE)⁴⁸ for the exchange correlation (xc)-functional.⁴⁹ The dependence of the QP G_0W_0 DOS and PDOS on the DFT xc-functional has been tested for 1ML intact H₂O@Ti_{cus} of stoichiometric TiO₂(110) and 1/2ML dissociated H₂O@O_{br}^{vac} of defective TiO_{2-1/4}(110) with 1/2ML of O_{br}^{vac}. For these structures, G_0W_0 calculations based on the local density approximation (LDA),⁵⁰ van der Waals (vdW-DF),⁵¹ and the range-separated hybrid (HSE)⁵² xc-functionals have been carried out for comparison with the PBE based G_0W_0 calculations. In particular, we use the HSE06⁵³ variant of the HSE xc-functional.

In the QP G_0W_0 approach, the contribution to the Kohn–Sham (KS) eigenvalues from the exchange and correlation (xc)-potential V_{xc} is replaced by the self-energy $\Sigma = iGW$, where G is the Green’s function and W is the screening⁴⁴ based on the KS wave functions.⁴⁵ The dielectric function is obtained from linear response time-dependent (TD) density functional theory (DFT) within the random phase approximation (RPA), including local field effects.⁴⁶ From G_0W_0 one obtains first-order QP corrections to the KS eigenvalues but retains the KS wave functions. Since our aim is to compare the computed interfacial level alignment with measured UPS spectra, it is most consistent to align the QP G_0W_0 levels with the VBM.

We find E_{vac} i.e., the effective potential far from the surface, from G_0W_0 is essentially the same as the E_{vac} from DFT. In other words, the effective potential is unchanged by G_0W_0 . To obtain a more accurate absolute QP level alignment relative to E_{vac} , we employ a self-consistent QP GW approach.⁴¹ In particular, by employing the scQPGW1 approach, we obtain

both a QP PDOS comparable to that from QP G_0W_0 and an improved alignment relative to E_{vac} .^{22,23} Here, 25%, 25%, and 50%, of the QP self-energies are “mixed” with the DFT xc-potential over three self-consistent QP GW cycles,⁴¹ respectively. If, instead, 100% of the DFT xc-potential were replaced by QP self-energy in a single self-consistent QP GW cycle, one would exactly obtain the QP G_0W_0 eigenvalues. However, this mixing is required to obtain a smooth convergence of both the QP wave functions and the absolute QP level alignment. To fully converge our self-consistent QP GW calculations (scQPGW), we perform a further eight cycles, with each introducing a further 25% of the QP self-energy.

The geometries have been fully relaxed using LDA,⁵⁰ PBE,⁴⁸ or vdW-DF⁵¹ xc-functionals, with all forces $\lesssim 0.02$ eV/Å. HSE calculations are performed for the relaxed geometries obtained with PBE. We employ a plane-wave energy cutoff of 445 eV, an electronic temperature $k_B T \approx 0.2$ eV with all energies extrapolated to $T \rightarrow 0$ K, and a PAW pseudopotential for Ti which includes the $3s^2$ and $3p^6$ semicore levels. All calculations have been performed spin unpolarized.

For the clean stoichiometric $TiO_2(110)$ surface²³ we have used a four layer slab and an orthorhombic 1×1 unit cell of $6.497 \times 2.958 \times 40$ Å³, i.e.,

$$\begin{pmatrix} \sqrt{2}a & 0 & 0 \\ 0 & c & 0 \\ 0 & 0 & \sqrt{2}a + D \end{pmatrix} \quad (1)$$

where $D \approx 27$ Å is the vacuum thickness, and a and c are the experimental lattice parameters for bulk rutile TiO_2 ($a = 4.5941$ Å, $c = 2.958$ Å).⁵⁴ We have employed a Γ -centered $4 \times 8 \times 1$ k-point mesh, and 320 bands = $9^{1/3}$ unoccupied bands per atom, i.e. including all levels up to 26 eV above the valence band maximum (VBM).

For the clean reduced $TiO_{2-1/4}(110)$ surface we have used a monoclinic 1×2 unit cell of $6.497 \times 5.916 \times 40$ Å³, i.e.,

$$\begin{pmatrix} \sqrt{2}a & c & 0 \\ 0 & 2c & 0 \\ 0 & 0 & \sqrt{2}a + D \end{pmatrix} \quad (2)$$

to maximize the separation between the O_{br}^{vac} . For the H_2O covered surfaces, we have employed a four layer slab with adsorbates on both sides and an orthorhombic 1×2 unit cell of $6.497 \times 5.916 \times 47$ Å³, i.e.,

$$\begin{pmatrix} \sqrt{2}a & 0 & 0 \\ 0 & 2c & 0 \\ 0 & 0 & \sqrt{2}a + D \end{pmatrix} \quad (3)$$

where $D \approx 34$ Å. We employed a Γ centered $4 \times 4 \times 1$ k-point mesh, with approximately $9^{1/6}$ unoccupied bands per atom, i.e. including all levels up to 30 eV above the VBM, an energy cutoff of 80 eV for the number of G-vectors, and a sampling of 80 frequency points for the dielectric function. The G_0W_0 parameters are consistent with those previously used for describing rutile TiO_2 bulk, $TiO_2(110)$ clean surface and interfaces.^{22,23} These parameters have been shown to provide accurate descriptions of bulk optical absorption spectra and both clean surface and interfacial level alignment.^{22,23}

To model H_2O in the gas phase, we employed a unit cell with C_{2v} symmetry and 16 Å of vacuum in each direction. At

the G_0W_0 level, we used a smaller energy cutoff of 40 eV for the number of G-vectors, which has previously shown to provide an accurate description of the optical absorption spectra for isolated molecules.^{55,56}

To obtain DFT total energies and the relaxed structure of the clean reduced $TiO_{2-1/8}(110)$ we have used a monoclinic 1×4 unit cell of $6.497 \times 11.832 \times 28$ Å³, i.e.,

$$\begin{pmatrix} \sqrt{2}a & 2c & 0 \\ 4c & 0 & \\ 0 & 0 & \sqrt{2}a + D \end{pmatrix} \quad (4)$$

where $D \approx 15$ Å, and employed a Γ -centered $4 \times 2 \times 1$ k-point mesh.

In this study, we have performed PBE and subsequent single-point RPBE⁵⁷ based DFT calculations for the H_2O adsorption energies E_{ads} on the stoichiometric and reduced surfaces. The RPBE xc-functional was especially developed for the prediction of adsorption properties on metal surfaces.⁵⁷ The H_2O adsorption energy on the Ti_{cus} site of a stoichiometric $TiO_2(110)$ surface is given by

$$E_{ads} \approx \frac{E[nH_2O + TiO_2(110)] - E[TiO_2(110)]}{n} - E[H_2O] \quad (5)$$

where n is the number of adsorbed H_2O functional units in the supercell, and $E[nH_2O + TiO_2(110)]$, $E[TiO_2(110)]$, and $E[H_2O]$ are the total energies of the covered and clean stoichiometric surfaces and gas phase water molecule, respectively. Similarly, the H_2O adsorption energy on the O_{br}^{vac} site of a reduced $TiO_{2-x}(110)$ surface is given by

$$E_{ads} \approx \frac{E[nH_2O + TiO_{2-x}(110)] - E[TiO_{2-x}(110)]}{n} - E[H_2O] \quad (6)$$

where $E[nH_2O + TiO_{2-x}(110)]$ and $E[TiO_{2-x}(110)]$ are the total energies of the covered and clean reduced surfaces, respectively.

3. RESULTS AND DISCUSSION

3.1. Intact H_2O on the Stoichiometric Surface. In Figure 1 we disentangle adsorbate and substrate contributions to the spectrum of intact $H_2O@Ti_{cus}$ and compare the H_2O PDOS to the theoretical and experimental difference DOS. Specifically, we model a monolayer (ML) of H_2O molecules with parallel (\rightarrow) interfacial hydrogen bonds aligned along the [001] direction (Figure 1(b)).^{58,59} Note that 1ML of intact H_2O is the most stable coverage and structure on the stoichiometric rutile $TiO_2(110)$ surface.³²

The theoretical difference DOS is the difference between the total DOS of the H_2O covered ($H_2O@Ti_{cus}$) and clean stoichiometric ($TiO_2(110)$) surfaces, as shown schematically in Figure 1(a). Turquoise areas in the $H_2O@Ti_{cus}$ and difference DOS indicate regions of greater density for the H_2O covered versus clean stoichiometric surface. The gray area indicates the DOS energy range for the clean stoichiometric $TiO_2(110)$ surface. Figure 1(c) and (d) shows two sets of UPS difference spectra obtained either by raising the temperature (from 150 to 190 K) for a consistent exposure to H_2O (0.2 L) for an annealed $TiO_2(110)$ surface²⁵ (Figure 1(c)) or by

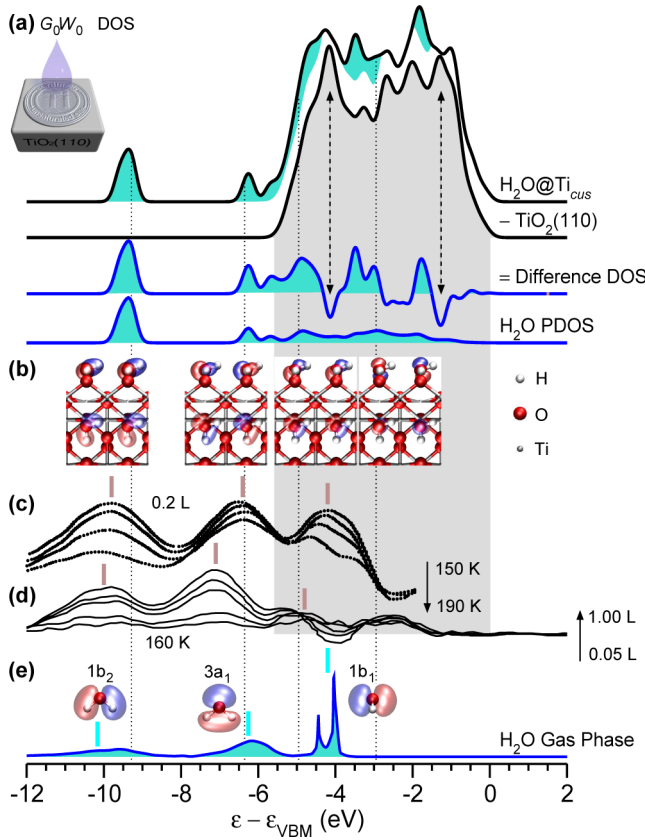


Figure 1. Intact H_2O adsorbed with parallel ($\overrightarrow{\text{H}}$) interfacial hydrogen bonds on coordinately unsaturated Ti sites ($\text{H}_2\text{O}@\text{Ti}_{\text{cus}}$). (a) G_0W_0 DOS for 1ML of intact H_2O covered (turquoise regions) or clean (gray region) stoichiometric $\text{TiO}_2(110)$, their total DOS difference (dashed line), and the H_2O PDOS. (b) Selected molecular orbitals at Γ and their energies (dotted lines). UPS difference spectra for H_2O covered $\text{TiO}_2(110)$ (c) after 0.2 L exposure for $T = 150, 160, 175$, and 190 K^{25} and (d) for $T = 160 \text{ K}$ after 0.05, 0.1, 0.3, 0.7, and 1 L exposure.¹⁸ Peak positions^{18,25} are marked in brown. (e) H_2O molecular orbitals, G_0W_0 calculated eigenenergies marked in cyan, and experimental gas phase spectrum aligned with the 1b_1 level of (c).³⁷ Energies are relative to the VBM (ϵ_{VBM}). Intensity references are provided for $\epsilon > \epsilon_{\text{VBM}}$ when available.

increasing the H_2O dose (from 0.01 to 1 L) at low temperature (160 K) for a nearly perfect surface¹⁸ (Figure 1d). The experimental spectra have been referenced to the VBM, which is positioned 3.2 eV below the experimental Fermi level.²³

Comparing the difference DOS to the H_2O PDOS, we find the peaks lying outside the $\text{TiO}_2(110)$ DOS energy range are clearly attributable to H_2O levels. As shown in Figure 1(b), these levels are related to the 1b_2 and 3a_1 H_2O orbitals shown in Figure 1e. This is not the case within the $\text{TiO}_2(110)$ DOS region, where the adsorbate levels are broadened by hybridization with the surface. This hybridization with the surface has been severely underestimated by previous cluster-based MP2 calculations.⁶⁰ Within the $\text{TiO}_2(110)$ DOS region, the peaks in the H_2O PDOS have corresponding peaks in the difference DOS, although the relative peak intensities differ substantially between the two methods. More importantly, the difference DOS has dips centered at $-4.1, -2.4$, and -1.1 eV , where there are adsorbate levels in the PDOS, and a peak at -0.4 eV , where there are no adsorbate levels in the PDOS. The dips at -4.1 and -1.1 eV correspond to the $\text{O } 2\text{p}_\sigma$ and $\text{O } 2\text{p}_\pi$ peaks in the $\text{TiO}_2(110)$ DOS,⁶¹ respectively, as marked in Figure 1(a).

These peaks split due to mixing with the 3a_1 and 1b_1 H_2O orbitals. This splitting is the origin of the observed dips in the difference DOS, which are also seen experimentally in Figure 1(c) and d.

The peak at -9.4 eV in the H_2O PDOS, which has 1b_2 molecular character, agrees semiquantitatively with the most strongly bound experimental peaks at -9.8 eV (Figure 1(c)) or -10.0 eV (Figure 1d). The peak at -6.3 eV in the H_2O PDOS, which has intermolecular 3a_1 bonding character, agrees semiquantitatively with the experimental peaks at -6.4 eV (Figure 1(c)) or -7.1 eV (Figure 1d). Note that the theoretical average deviation is within that among the experiments. This may reflect differences in sample preparation, which result in a variety of different H_2O configurations, i.e., H_2O coverages, $\text{O}_{\text{br}}^{\text{vac}}$ concentrations, and mixtures of intact and dissociated H_2O . As we will show in Section 3.4, by considering a variety of H_2O structures a more complete description of the experiment is obtained. Altogether, this agreement for the -9.4 and -6.3 eV PDOS peaks lends confidence to our results for regions where the experimental results are unclear.

The assignment of the peaks located within the $\text{TiO}_2(110)$ DOS is much more complicated. The assumption that the highest peak in the experimental spectra originates solely from the $\text{H}_2\text{O} 1\text{b}_1$ level^{25,26} is an oversimplification. In fact, both the 3a_1 and 1b_1 molecular levels contribute within this region (Figure 1(b)). While the levels with intermolecular 3a_1 bonding character give rise to a distinct peak below the $\text{TiO}_2(110)$ DOS region, those with intermolecular 3a_1 antibonding character are pushed to higher energies and mixed with the 1b_1 molecular levels (Figure 1(b)). The latter is due to symmetry breaking at the interface. Consequently, the H_2O PDOS is broadened into several peaks between -5 and -1 eV . These levels have interfacial ($3\text{a}_1/1\text{b}_1 - \text{O } 2\text{p}_\sigma/2\text{p}_\pi$) bonding and antibonding character (not visible at the isosurface value used).

3.2. Dissociated H_2O on Reduced Surfaces. To see how dissociation of $\text{H}_2\text{O}@\text{O}_{\text{br}}^{\text{vac}}$ affects the spectrum, we now consider $1/2\text{ML}$ of H_2O dissociated on a reduced $\text{TiO}_{2-1/4}(110)$ surface (Figure 2). Here, we have used $\text{TiO}_{2-1/4}(110)$ to denote a surface consisting of $1/2\text{ML}$ of $\text{O}_{\text{br}}^{\text{vac}}$ defects. This structure corresponds to the staggered $\text{O}_{\text{br}}\text{H}$ surface species, shown in Figure 2(b).

The theoretical difference DOS is the difference between the total DOS of the H_2O covered ($\text{H}_2\text{O}@\text{O}_{\text{br}}^{\text{vac}}$) and the clean reduced ($\text{TiO}_{2-1/4}(110)$) surfaces, shown schematically in Figure 2(a). Turquoise areas in the $\text{H}_2\text{O}@\text{O}_{\text{br}}^{\text{vac}}$ and difference DOS indicate regions of greater density for the H_2O covered versus clean reduced surface. The gray area indicates the DOS energy range for the clean reduced $\text{TiO}_{2-1/4}(110)$ surface. The $\text{O}_{\text{br}}^{\text{vac}}$ defects give rise to occupied levels with Ti 3d character that are just below the conduction band minimum and outside the energy range shown.^{62–64} Note that the H_2O PDOS includes half the O atoms and all the H atoms that make up the $\text{O}_{\text{br}}\text{H}$ species. In this way the PDOS is provided in terms of H_2O formula units.

The peak in the difference DOS and PDOS at -7.0 eV has $\text{O}_{\text{br}}\text{H } \sigma$ character, as shown in Figure 2(b). Note that the peak intensity in the PDOS is about half that in the difference DOS, as the PDOS includes half the O_{br} atoms. This peak's position agrees semiquantitatively with the experimental peaks at -7.1 (Figure 2(c)), -7.6 (Figure 2d), or -7.2 eV (Figure 2e). The PDOS has a broader feature between -4 and -1 eV , due to hybridization with the surface. This feature is associated with

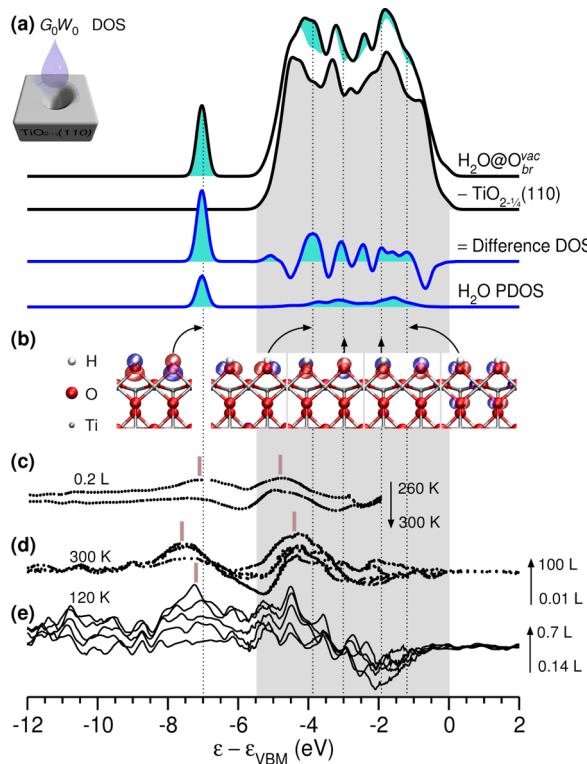


Figure 2. H_2O dissociated on bridging O vacancies ($\text{H}_2\text{O}@O_{br}^{vac}$). (a) G_0W_0 DOS for $1/2\text{ML}$ of dissociated H_2O covered (turquoise regions) or clean (gray region) defective $\text{TiO}_{2-1/4}(110)$ with $1/2\text{ML}$ of O_{br}^{vac} , their total DOS difference (dashed line), and the H_2O PDOS. (b) Selected molecular orbitals and their energies (dotted lines). UPS difference spectra for H_2O on reduced $\text{TiO}_{2-x}(110)$ (c) after 0.2 L exposure for $T = 260$ and 300 K ,²⁵ (d) for $T = 300 \text{ K}$ after between 0.01 and 100 L exposure,¹⁸ and (e) for $T = 120 \text{ K}$ after 0.14 , 0.3 , 0.4 , 0.5 , and 0.7 L exposure.²⁶ Peak positions^{18,25,26} are marked in brown. Energies are relative to the VBM (ϵ_{VBM}). Intensity references are provided for $\epsilon > \epsilon_{VBM}$ when available.

contributions coming from the bonding and antibonding combinations of two distinct p orbitals of the $O_{br}\text{H}$ species (Figure 2(b)): one perpendicular to the $O_{br}\text{H}$ σ bonds (the so-called OH π level of NaOH³⁸); the other in the plane of the $O_{br}\text{H}$ σ bonds. The lowest of these peaks at -3.9 eV corresponds to the bonding combination of the $O_{br}\text{H}$ π levels. This peak's position agrees semiquantitatively with the consistently observed experimental peaks at -4.8 , -4.4 , and -4.5 eV in Figures 2(c), 2d, and 2e, respectively. However, the antibonding $O_{br}\text{H}$ π levels are shifted to much higher energies (-1.2 eV), as shown in Figure 2(b).

Much of the theoretical difference DOS's structure is attributable to the defect healing of O_{br}^{vac} , as seen from the difference DOS between $\text{TiO}_2(110)$ and $\text{TiO}_{2-1/4}(110)$ in Figure 3. This suggests that the observed features in the experimental difference spectra overlapping with the reduced surface's DOS are simply O_{br} levels reintroduced by dissociated $\text{H}_2\text{O}@O_{br}^{vac}$. In particular, the peak which is usually attributed to $O_{br}\text{H}$ π levels is actually composed of O_{br} surface levels unrelated to the presence of H atoms.

3.3. XC-Functional and Methodology Dependence of H_2O Spectra for Stoichiometric and Reduced Surfaces. To assess the robustness of the calculated QP H_2O PDOS, we consider its dependence on the xc-functional and methodology. Specifically, we compare the H_2O PDOS from DFT,

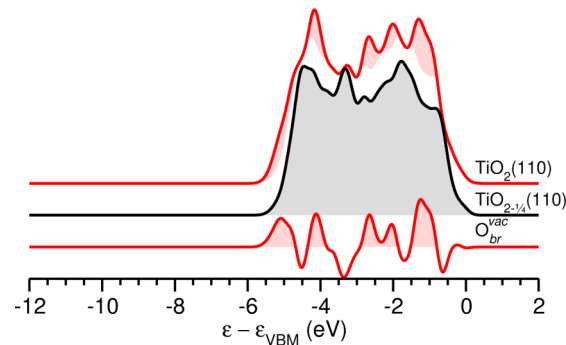


Figure 3. O_{br}^{vac} difference DOS between (red) stoichiometric $\text{TiO}_2(110)$ and (black) reduced $\text{TiO}_{2-1/4}(110)$ with $1/2\text{ML}$ of O_{br}^{vac} defects. Red areas indicate defect healing of O_{br}^{vac} , i.e., regions of greater density for the stoichiometric versus reduced surfaces, shown in Figures 7 and 8, respectively.

scQPGW1, and G_0W_0 for $1/2\text{ML}$ intact $\text{H}_2\text{O}@Ti_{cus}$ with parallel (\rightarrow) and antiparallel (\leftrightarrow) interfacial hydrogen bonds and $1/2\text{ML}$ dissociated $\text{H}_2\text{O}@O_{br}^{vac}$ in Figures 4, 5, and 6, respectively.

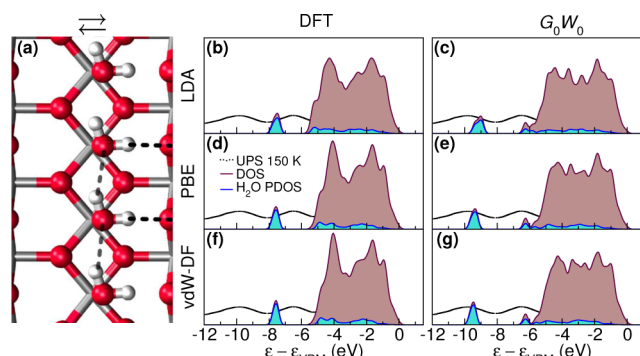


Figure 4. (a) 1ML intact H_2O adsorbed with parallel (\rightarrow) interfacial hydrogen bonds (black dashed lines) on coordinately unsaturated Ti sites ($\text{H}_2\text{O}@Ti_{cus}$). Total (maroon) and H_2O projected (blue) DOS computed with (b,d,f) DFT and (c,e,g) G_0W_0 using the (b,c) local density approximation (LDA),⁵⁰ (d,e) generalized gradient approximation (PBE),⁴⁸ and (f,g) long-ranged van der Waals interactions (vdW-DF)⁵¹ for the xc-functional. The calculated H_2O PDOS are compared with the UPS spectrum at 150 K after 0.2 L exposure²⁵ (black). Energies are relative to the valence band maximum, ϵ_{VBM} .

We find the observed structure of the G_0W_0 H_2O PDOS is independent of whether the local density approximation (LDA),⁵⁰ generalized gradient approximation (PBE),⁴⁸ long-ranged van der Waals interactions (vdW-DF),⁵¹ or a range-separated hybrid (HSE06)⁵³ are employed for the xc-functional. This is consistent with the previously reported similarities between PBE and HSE based G_0W_0 PDOS for CH_3OH on $\text{TiO}_2(110)$.²³ This is despite the greater differences observed among the DFT H_2O PDOS, which all differ qualitatively from the experiments. Furthermore, the G_0W_0 H_2O PDOS is robust to the resulting changes in the H_2O height above the surface, i.e., the distance between H_2O and Ti_{cus} $d[\text{H}_2\text{O}-\text{Ti}_{cus}]$, shown in Table 1. Furthermore, Figure 5(d,e) shows that scQPGW1 provides a similar H_2O PDOS level alignment to G_0W_0 . This is consistent with what was previously reported for the $\text{CH}_3\text{OH}-\text{TiO}_2(110)$ interface.^{22,23}

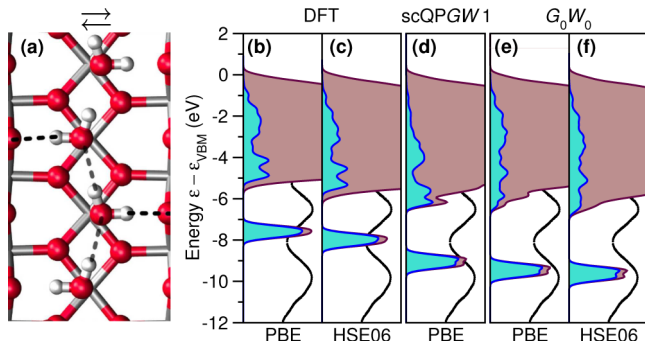


Figure 5. (a) 1ML intact H₂O adsorbed with antiparallel (\rightleftharpoons) interfacial hydrogen bonds on coordinately unsaturated Ti sites (H₂O@Ti_{cu}). Total (maroon) and H₂O projected (blue) DOS computed with (b,c) DFT, (d) scQPGW1, and (e,f) G₀W₀ using the (b,d,e) generalized gradient approximation (PBE)⁴⁸ and (c,f) range-separated hybrid (HSE06)⁵³ for the xc-functional. The calculated H₂O PDOS are compared with the UPS spectrum at 150 K after 0.2 L exposure²⁵ (black). Energies are relative to the valence band maximum, ϵ_{VBM} .

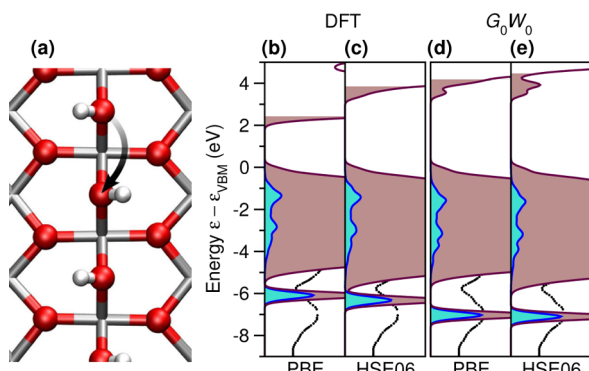


Figure 6. (a) 1/2ML H₂O dissociated on bridging O vacancies (H₂O@O_{br}^{vac}) of defective TiO_{2-1/4}(110) with 1/2ML of O_{br}^{vac}. Total (maroon) and H₂O projected (blue) DOS computed with (b,c) DFT and (d,e) G₀W₀ using the (b,d) generalized gradient approximation (PBE)⁴⁸ and (c,e) range-separated hybrid (HSE06)⁵³ for the xc-functional. Filling denotes occupation. The calculated H₂O PDOS are compared with the UPS spectrum at 300 K after 0.2 L exposure²⁵ (black). Energies are relative to the valence band maximum, ϵ_{VBM} .

Table 1. Height of H₂O Above TiO₂(110) for 1ML Intact H₂O@Ti_{cu} Measured with SXPS and Calculated with LDA, PBE, or vdW-DF XC-Functionals

method	$d[\text{H}_2\text{O}-\text{Ti}_{cu}]$ (Å)
SXPS ^{65,66}	2.210
LDA	2.180
PBE	2.367
vdW-DF	2.434

We clearly see that the differences between the DFT and G₀W₀ PDOS, i.e., the QP energy shifts, are far from simply being rigid. For instance, we find for PBE that the QP energy shifts for the levels that contribute to the highest-energy PDOS peak ϵ_{peak}^{PDOS} are almost negligible (cf. Figures 4(d,e) and 5(b,e)). As a result, the QP G₀W₀ ϵ_{peak}^{PDOS} is only \sim 0.1 eV lower compared to DFT. On the other hand, we find significant QP shifts to stronger binding for the levels that contribute to the most strongly bound PDOS peak with 1b₂ σ molecular character. For example, with PBE the QP G₀W₀ lowest energy peak is shifted

by $\sim - 1.7$ eV compared to DFT (cf. Figures 4(d,e) and 5(b,e)).

As previously shown for the CH₃OH–TiO₂(110) interface, these differences in the shifts of the peaks are directly related to differences in the spatial distribution of the wave functions for the levels contributing to the peaks.^{22–24} This is because the QP G₀W₀ corrections to the DFT eigenenergies for interfaces are directly correlated with the spacial distribution of the wave functions.^{22–24} The negligible shift of the DFT highest-energy PDOS peak (Figures 4 (b,d,f) and 5(b,c)) is due to its strong hybridization with the surface, i.e., weight on TiO₂(110), for the levels contributing to this peak.^{22–24} On the other hand, the levels that contribute to the most strongly bound PDOS peak have little weight on TiO₂(110) and have σ character. Both their localized H₂O character as well as their σ nature explain why these levels have large QP energy shifts to stronger binding.^{22–24}

Oxygen defective and hydroxylated (*h*–)TiO₂ surfaces have occupied 3d levels which are associated with reduced Ti³⁺ atoms.⁶⁴ One such example is the 1/2ML dissociated H₂O@O_{br}^{vac} on reduced TiO_{2-1/4}(110) with 1/2ML of O_{br}^{vac} shown in Figure 6(a). The spacial distribution of the 3d density for O defective surfaces has been characterized by low temperature scanning tunneling microscopy (STM).^{63,67} STM measurements find at 77 K the 3d density is homogeneously distributed along the [100] direction,⁶³ while at \sim 5 K the 3d density exhibits an asymmetric localized character.⁶⁷

A localized description of the Ti³⁺ occupied 3d levels is not obtained from DFT with standard xc-functionals. For example, the occupied 3d levels obtained with PBE are highly delocalized, as clearly shown in Figure 6(b). This is due to self-interaction errors which are inherent in such xc-functionals. If one performs spin-polarized DFT calculations with a hybrid xc-functional on such systems, one obtains localized Ti³⁺ 3d¹ levels between 0.7 and 1.6 eV below the CBM, along with a structural deformation of the TiO₂(110) surface.^{63,64} However, spin-paired calculations with HSE06 on the PBE relaxed geometry only yield an occupied shoulder at the CBM (Figure 6(c)). At the QP G₀W₀ level based on PBE, this shoulder evolves into a distinct peak about 0.6 eV below the Fermi level, ϵ_F . This effect is even more pronounced when the G₀W₀ calculation is based on HSE06 (cf. Figure 6(d,e)), which yields peaks at 0.6 and 0.9 eV below ϵ_F . As compared to G₀W₀ PBE, G₀W₀ HSE06 shifts the unoccupied 3d levels further up in energy revealing the double peak structure. These energies are in very good agreement with the peak at 0.8 eV below ϵ_F in the UPS spectra of H₂O@O_{br}^{vac} of Figure 2(d). This peak is not shown in Figure 2(d) as it is slightly above 2 eV with respect to VBM.¹⁸ However, note that G₀W₀ overestimates by about 1 eV the VBM position relative to ϵ_F as compared with UPS experiments.¹⁸

This result is completely independent of the wave function's spacial distribution, i.e., localization, as the G₀W₀ calculations are based on the KS wave functions. This is different from previous findings, which showed DFT with either PBE or hybrid xc-functionals is only giving distinct peaks for the occupied 3d levels provided the relaxed spin-polarized distorted structure is used in the calculations.^{63,64}

While for G₀W₀ based on PBE and HSE06 one sees noticeable differences in the description of the 3d occupied levels, the QP H₂O PDOS and its alignment relative to the VBM are unchanged. Although localization of the Ti³⁺ occupied

levels and associated structural deformations are absent from our approach, such features should not significantly alter the QP H₂O PDOS. This is because the Ti³⁺ levels are too far above the VBM (~ 2 eV⁶⁴) to hybridize with the H₂O. Moreover, as we will show in Section 3.4, the QP H₂O PDOS is rather robust to local deformations of the surface structure, e.g., due to changes in coverage.

3.4. Coverage and Dissociation Dependence of H₂O Spectra for Stoichiometric and Reduced Surfaces. As different experimental conditions and surface preparations have been employed, there are expected to be different H₂O structures on the surface. To evaluate how strongly the DOS depends on the adsorption geometry, we now consider a variety of coverages of intact and dissociated H₂O on rutile stoichiometric TiO₂(110) (Figure 7) and reduced

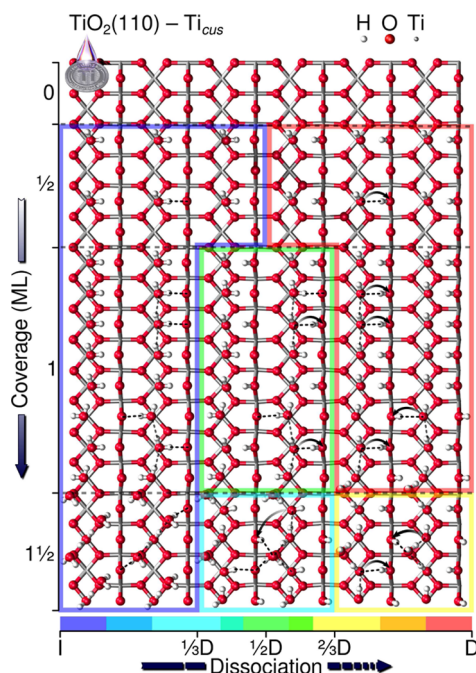


Figure 7. Schematics of H₂O adsorbed intact (I) or dissociated (D) on coordinately unsaturated Ti sites (Ti_{cus}) of stoichiometric TiO₂(110). Higher coverages are obtained by the addition of second-layer H₂O. Coverage is the number of H₂O formula units per (110) 1×1 unit area of the clean stoichiometric surface. Dissociation is the fraction of H₂O molecules which are dissociated, i.e., one minus the ratio of intact H₂O molecules to H₂O formula units. Colored frames encompass regions of common fractional dissociation. Charge transfer of about $-0.4e$ accompanying deprotonation²² of intact H₂O adsorbed at Ti_{cus} is represented by arrows, while intermolecular (gray) and interfacial (black) hydrogen bonds are denoted by dotted lines.

TiO_{2-1/4}(110) (Figure 8) and TiO_{2-1/8}(110) (Figure 9) with $1/2$ ML and $1/4$ ML of O_{br}^{vac} defects, respectively. The relative importance of these geometries is illustrated in Figure 10(a) and 10(b) by the average absorption energy E_{ads} per H₂O molecule on the stoichiometric or reduced surfaces⁶⁸ with either PBE⁴⁸ or RPBE⁵⁷ xc-functionals. In so doing, the contribution of different structures to the measured spectra can be disentangled. Note that an intact $1/2$ ML of H₂O@O_{br}^{vac} (Figure 8(b)) is probably only a transient locally stable state of the reduced H₂O-TiO_{2-1/4}(110) interface,²⁹ which may easily evolve into the ~ 0.7 eV more stable dissociated $1/2$ ML H₂O@

O_{br}^{vac} (Figure 8(c)). For this reason, we only consider dissociated H₂O@O_{br}^{vac} structures in Figure 10d.

By comparing to lower coverage H₂O structures ($1/2$ ML^{30-32,69} to $1^{1/2}$ ML^{30-32,69} in Figure 7 and $1/4$ ML⁷⁰ in Figure 9 to $1/2$ ML⁷¹ in Figure 8), we can disentangle the effect of interaction between the H₂O molecules on the spectra. Further, these structures allow us to probe the isolated molecule limit.

As shown in Figure 10, at lower coverages the overall width of the spectra is reduced with fewer distinct peaks. When the coverage is increased to include intermolecular interactions between adjacent species, the molecular levels hybridize into bonding and antibonding intermolecular levels. This produces additional peaks above and below those present at low coverage. As a result, the peak with intermolecular bonding 3a₁ character at -6.3 eV for 1ML of H₂O@Ti_{cus} is absent for a $1/2$ ML coverage. This reinforces the assignment of the experimental spectra shown in Figure 1 to an intact 1ML H₂O@Ti_{cus} geometry with interacting molecules.

To see how the spectra for dissociation of H₂O@Ti_{cus} compare to H₂O@O_{br}^{vac}, we have considered the half-dissociated (12D) and fully dissociated (D) H₂O structures shown in Figure 7. As shown in Figure 10(c), the peak at -7.0 eV with O_{br}H σ character for H₂O@O_{br}^{vac} splits into two peaks for dissociated H₂O@Ti_{cus}. The lower energy peak has both O_{cus}H and O_{br}H σ character, while the higher energy peak is mostly O_{cus}H in character. Furthermore, we find a similar couple of peaks for $3/4$ ML mixtures of dissociated H₂O@Ti_{cus} and H₂O@O_{br}^{vac} shown in Figure 10d. This means one may recognize dissociated H₂O@Ti_{cus} by both the presence of two peaks at about -7.0 and -6.3 eV and the absence of the low-energy peak with 1b₂ character for intact H₂O@Ti_{cus}.

The absence of a peak at about -6.3 eV in the experimental spectra shown in Figure 2(c) reinforces its attribution to dissociated H₂O@O_{br}^{vac} rather than dissociated H₂O@Ti_{cus}. This is further supported by the calculated H₂O absorption energies (Figure 10(a) and 10(b)). These are generally weaker for dissociated H₂O@Ti_{cus}²⁹ and stronger for H₂O@O_{br}^{vac}, as in previous calculations.

To check whether changes in the absorption geometry of H₂O affect the spectra for the same coverage, we compare 1ML of H₂O {I, $1/2$ D, D} adsorbed with either parallel (\rightarrow) or antiparallel (\leftrightarrow) interfacial hydrogen bonds⁵⁸ (black dashed lines in Figure 7). Overall, the two sets of spectra are consistent and demonstrate the general robustness of the DOS to minor changes in the water absorption geometry. However, as the H₂O molecules are no longer equivalent when the interfacial hydrogen bonds are antiparallel, there is a greater splitting between bonding and antibonding contributions for the peaks with 1b₂ and 3a₁ molecular character. In particular, for intact H₂O, the lowest energy peak with molecular 1b₂ character splits with a separate peak at -9.6 eV, which is closer to the peaks at -9.8^{25} (Figure 1(c)) and -10.0 eV¹⁸ (Figure 1d) observed experimentally.

To see how increasing the H₂O coverage impacts the spectra, we compare monolayer ($1/2$ ML or 1ML) to multilayer ($1^{1/2}$ ML) H₂O {I, $1/3$ D, $2/3$ D}⁷² (Figure 7) and consider the effect of additional H₂O@Ti_{cus} to $1/4$ ML (Figure 9) and $1/2$ ML (Figure 8) H₂O@O_{br}^{vac}.⁶⁹ In this way we can see how robust the observed features in the individual spectra for isolated species are to screening by H₂O layers^{6,7} and probe the liquid water limit.⁷³

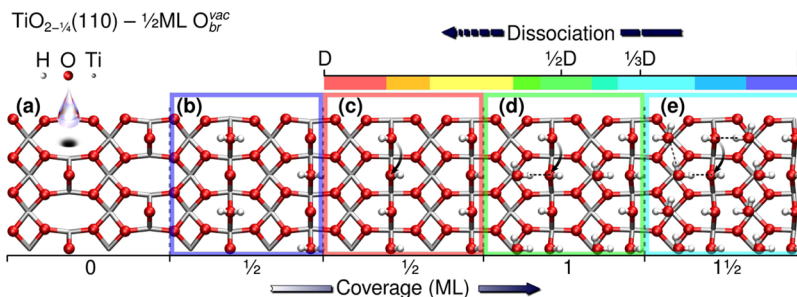


Figure 8. Schematics of reduced $\text{TiO}_{2-\frac{1}{4}}(110)$ with $\frac{1}{2}\text{ML}$ of bridging O vacancies ($\text{O}_{\text{br}}^{\text{vac}}$) (a) clean, covered with $\frac{1}{2}\text{ML}$ (b) intact and (c) dissociated $\text{H}_2\text{O}@_{\text{br}}^{\text{vac}}$, and with an additional (d) $\frac{1}{2}\text{ML}$ or (e) 1ML of intact H_2O adsorbed on coordinately unsaturated Ti sites (Ti_{cus}). Coverage is the number of H_2O formula units per (110) 1×1 unit area of the clean reduced surface. Dissociation is the fraction of H_2O molecules which are dissociated, i.e., one minus the ratio of intact H_2O molecules to H_2O formula units. Charge transfer of about -0.4e accompanying deprotonation²² is represented by arrows, while intermolecular (gray) and interfacial (black) hydrogen bonds are denoted by dotted lines.

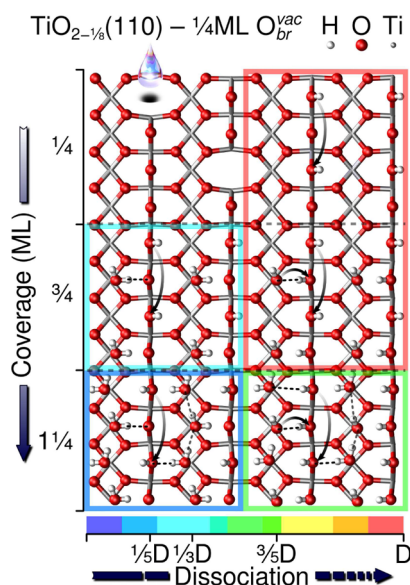


Figure 9. Schematics of H_2O adsorbed dissociated (D) on $\frac{1}{4}\text{ML}$ of bridging O vacancies ($\text{O}_{\text{br}}^{\text{vac}}$) on reduced $\text{TiO}_{2-x}(110)$ ($x = \frac{1}{8}$). Higher coverages are obtained by the addition of $\text{H}_2\text{O}@_{\text{Ti}_{\text{cus}}}$. Coverage is the number of H_2O formula units per (110) 1×1 unit area of the clean stoichiometric or reduced surface. Dissociation is the fraction of H_2O molecules which are dissociated, i.e., one minus the ratio of intact H_2O molecules to H_2O formula units. Colored frames encompass regions of common fractional dissociation. Charge transfer of about -0.4e accompanying deprotonation²² of intact H_2O adsorbed at Ti_{cus} or $\text{O}_{\text{br}}^{\text{vac}}$ is represented by arrows, while intermolecular (gray) and interfacial (black) hydrogen bonds are denoted by dotted lines.

When a second layer of H_2O is added to the low coverage intact $\frac{1}{2}\text{ML}$ $\text{H}_2\text{O}@_{\text{Ti}_{\text{cus}}}$ structure, the levels with H_2O 1b_2 character are unchanged, while the levels with 3a_1 and 1b_1 second layer character are more localized and weakly hybridized with the surface. These levels are seen as the two most intense peaks at -4.3 and -2.2 eV (Figure 10(c)). The former coincides with the peak at -4.2 eV observed experimentally at low temperatures (Figure 1(c)), suggesting multilayer H_2O structures may be present under these experimental conditions. The intermolecular H bonding between the layers delocalizes the molecular levels of the first layer. This is seen from the peak at -6.1 eV with antibonding 3a_1 character on the first layer. We saw the same behavior when increasing the first layer's coverage from $\frac{1}{2}\text{ML}$ to 1ML . This is further confirmation that the peak

observed experimentally at -6.4 eV has intermolecular character.

When a second $\frac{1}{2}$ layer of H_2O is added to the 1ML $\text{H}_2\text{O}@_{\text{Ti}_{\text{cus}}}$ $\{\frac{1}{3}\text{D}, \frac{2}{3}\text{D}\}$ structures,⁷² a denser network of intermolecular and interfacial hydrogen bonds is formed, as shown in Figure 7. This causes a stronger hybridization between the OH and H_2O σ levels. For the 13D structure, this results in the four distinct σ peaks shown in Figure 10(c). On the one hand, the peaks at -9.1 and -6.2 eV have predominantly intact H_2O and $\text{O}_{\text{cus}}\text{H}$ character, as was the case for 1ML of $\frac{1}{2}\text{D}$ $\text{H}_2\text{O}@_{\text{Ti}_{\text{cus}}}$. On the other hand, the peaks at -7.9 and -7.4 eV are most related to the second layer. In effect, the H_2O σ level of the second-layer H_2O , which is fully saturated with four hydrogen bonds, is upshifted by more than an eV.

This is not the case for the $\frac{2}{3}\text{D}$ structure (Figure 7), where the peak at -9.1 eV instead has mostly intact second-layer H_2O 1b_2 character. As was the case for intact $\frac{1}{2}\text{ML}$ $\text{H}_2\text{O}@_{\text{Ti}_{\text{cus}}}$, the addition of a second $\frac{1}{2}$ layer of H_2O induces a stronger hybridization of the $\text{O}_{\text{br}}\text{H}$ levels and introduces an additional intense peak at -4.4 eV (Figure 10(c)). This again suggests the experimentally observed peak at -4.2 eV (Figure 1(c)) may be due to multilayer H_2O .

Overall, we find the addition of second-layer H_2O affects the resulting spectrum qualitatively. We find both additional features and a redistribution of those due to the first H_2O layer. When we instead add $\text{H}_2\text{O}@_{\text{Ti}_{\text{cus}}}$ to the $\frac{1}{4}\text{ML}$ and $\frac{1}{2}\text{ML}$ $\text{H}_2\text{O}@_{\text{O}_{\text{br}}^{\text{vac}}}$ structures (Figures 9 and 8) we find the resulting spectrum is the sum of the separate spectra to within 0.2 eV (Figure 10). For example, the $\frac{1}{2}\text{ML}$ $\frac{1}{3}\text{D}$ spectrum (Figure 10(d)) for 1ML of intact H_2O added to $\frac{1}{2}\text{ML}$ $\text{H}_2\text{O}@_{\text{O}_{\text{br}}^{\text{vac}}}$ (Figure 8) is basically the sum of the 1ML intact $\text{H}_2\text{O}@_{\text{Ti}_{\text{cus}}}$ (Figure 1(a)) and $\frac{1}{2}\text{ML}$ $\text{H}_2\text{O}@_{\text{O}_{\text{br}}^{\text{vac}}}$ (Figure 2(a)) PDOS spectra downshifted by 0.2 eV. This explains the ease with which the experimental single-layer H_2O spectra may be analyzed for levels outside the surface DOS region.

3.5. Alignment of the Highest H_2O Occupied Levels.

So far, we have concentrated our analysis on the lower energy peaks observed in the experimental spectra. This was done to demonstrate the robustness of the calculated QP DOS. Having established this, we now focus on the adsorbate levels near the VBM, which play an important role in photooxidation processes. In this respect, the highest H_2O occupied levels' alignment for 1ML intact and dissociated $\text{H}_2\text{O}@_{\text{Ti}_{\text{cus}}}$ and $\frac{1}{2}\text{ML}$ dissociated $\text{H}_2\text{O}@_{\text{O}_{\text{br}}^{\text{vac}}}$ is of utmost importance. The former structure corresponds to the reactant species on

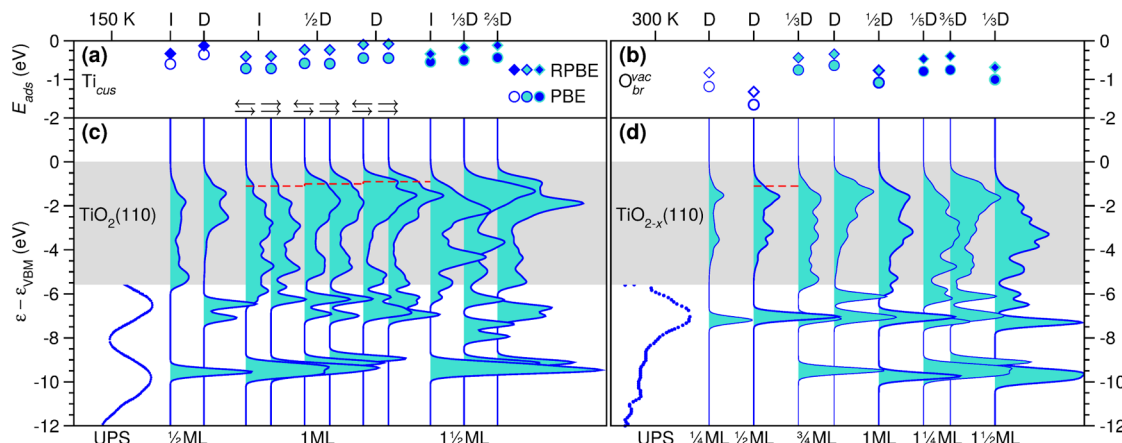


Figure 10. Structure and coverage dependence of (a,b) adsorption energy E_{ads} and (c,d) G_0W_0 PDOS for H_2O adsorbed intact (I) or dissociated (D) on (a,c) coordinately unsaturated Ti sites (Ti_{cus}) of stoichiometric $TiO_2(110)$ (Figure 7) and (b,d) bridging O vacancies (O_{br}^{vac}) of reduced $TiO_{2-x}(110)$, with $x = 18$ (thin lines, Figure 9) or 14 (thick lines, Figure 8). (a,b) E_{ads} calculated with PBE (○) and RPBE (◊) xc-functionals for (white) low ($1/4$ and $1/2$ ML), (turquoise) medium ($3/4$ and 1 ML), and (blue) high ($1 1/4$ and $1 1/2$ ML) coverage. UPS difference spectra at (c) 150 K and (d) 300 K after 0.2 L exposure are from ref 25. (c,d) Energies are relative to the VBM (ϵ_{VBM}). Gray regions denote the clean surface DOS. Red dashed lines denote the highest PDOS peaks (ϵ_{peak}^{PDOS}) for 1ML $H_2O@Ti_{cus}$ and $1/2$ ML $H_2O@O_{br}^{vac}$.

stoichiometric surfaces,³² which undergoes photoirradiation. The latter structures act as hole traps and are thus the main oxidizing agents on $TiO_2(110)$.^{74,75}

We have shown that the experimental peak at -4.2 eV²⁵ is not, in fact, the highest energy peak of $H_2O@Ti_{cus}$. We instead find the highest-energy PDOS peak, ϵ_{peak}^{PDOS} , for 1ML intact $H_2O@Ti_{cus}$ at -1.1 eV relative to the VBM (Figure 10(c)). This is 0.6 eV closer to the VBM than the ~ -1.7 eV estimate¹⁵ deduced from the onsets of the UPS difference spectra in ref 18. Moreover, as 1ML $H_2O@Ti_{cus}$ dissociates, ϵ_{peak}^{PDOS} moves up to -1.0 eV ($1/2$ D) and -0.9 eV (D) (Figure 10(c)). This is again significantly higher than the ~ -1.8 eV estimate⁷ based on UPS difference spectra for the $TiO_2(100)$ surface from ref 76. As was the case for CH_3OH on $TiO_2(110)$,²² this raising of ϵ_{peak}^{PDOS} can be related to the charge transfer of $-0.4e$ that accompanies deprotonation (arrows in Figure 7). We find for the 1ML intact structure on $TiO_2(110)$ ϵ_{peak}^{PDOS} is 0.2 eV closer to the VBM for H_2O than for CH_3OH ,^{22–24} while for the 1ML $1/2$ D structures ϵ_{peak}^{PDOS} is the same. However, the highest PDOS peak is both less intense and broader for H_2O compared to CH_3OH , due to the stronger hybridization with the surface. This is why, as discussed in Section 3.1, the QP G_0W_0 ϵ_{peak}^{PDOS} is only ~ 0.1 eV lower compared to DFT^{22–24} (Figure 4). After adding second-layer H_2O , ϵ_{peak}^{PDOS} is unchanged with weight mostly remaining on the first layer.

We find for $1/2$ ML dissociated $H_2O@O_{br}^{vac}$ $\epsilon_{peak}^{PDOS} \approx -1.1$ eV relative to the VBM (Figure 10d), the same as for intact $H_2O@Ti_{cus}$. This is much higher than the previous estimate of ~ -3.7 eV for $O_{br}H$ based on the UPS difference spectra in ref 25. Our corrected ϵ_{peak}^{PDOS} value agrees with the recently demonstrated photocatalytic importance of $O_{br}H$ sites as the main oxidizing species on $TiO_2(110)$.⁷⁴

Based on ϵ_{peak}^{PDOS} for 1ML intact $H_2O@Ti_{cus}$, vertical excitations from the highest H_2O occupied levels to the $TiO_2(110)$ conduction band require photon energies that exceed the electronic band gap for bulk rutile TiO_2 (3.3 ± 0.5 eV⁷⁷) by $\gtrsim 1$ eV. However, the hole generated by such supraband gap excitations should be mostly located on $TiO_2(110)$ O $2p_\pi$ rather than H_2O O $2p$ levels. This is because the H_2O highest levels are hybridized with $TiO_2(110)$ and are predominantly $TiO_2(110)$ in character.

The fact that the highest H_2O levels are ~ 1 eV below the VBM does not necessarily mean that they cannot be photooxidized by holes photogenerated within the $TiO_2(110)$ valence band. A recent DFT study with HSE06 found trapped holes at surface O sites, i.e., 3-fold coordinated O_{3fold} are shared with nearby H O-Ti_{cus} groups.⁵ Moreover, it has been suggested that H_2O can only be photooxidized, i.e., trap a hole, upon deprotonation.^{78,79} In other words, hole transfer to the HO-Ti_{cus} site should be mediated by the deprotonation of intact $H_2O@Ti_{cus}$ to the nearest O_{br} site. Altogether, this suggests that $H_2O@Ti_{cus}$ photooxidation should be initiated by band-to-band and supraband photoexcitations, which result in the generation of holes within the $TiO_2(110)$ valence band. These $TiO_2(110)$ free holes may then be trapped at O_{3fold} sites and partially transferred to nearby HO-Ti_{cus} upon H_2O deprotonation.

3.6. Vacuum Level Alignment. So far, we have considered the level alignment of the interfacial levels relative to the VBM of the substrate. This allows a direct comparison of the occupied PDOS with the measured UPS spectra. However, to assess the photoelectrocatalytic activity of the interface, one needs the absolute level alignment relative to the vacuum level E_{vac} .

In Figure 11 we show the level alignment for gas phase H_2O and 1ML intact $H_2O@Ti_{cus}$ relative to E_{vac} from DFT, scQPGW1, and G_0W_0 based on PBE and HSE xc-functionals. These are compared to the measured CBM for the liquid $H_2O-TiO_2(110)$ interface^{40,86} and the measured and coupled-cluster (CCSD(T)) gas phase H_2O ionization potential.⁸⁰

Our calculated IP values for H_2O in gas phase are consistent with those reported previously in the literature.^{80,87–89} Although the relative energies of the $1b_1$, $3a_1$, and $1b_2$ H_2O levels are consistent over all five levels of theory, the levels are rigidly downshifted. We observe a clear ordering in increasing IP of PBE DFT (7.2 eV) $<$ HSE DFT \ll PBE scQPGW1 $<$ PBE $G_0W_0 \lesssim$ HSE $G_0W_0 \lesssim$ PBE scQPGW (12.8 eV) $<$ Hartree-Fock (HF 13.9 eV⁸⁸).

To understand the origin of this ordering, we have probed the dependence of the IP on the fraction of Hartree-Fock exact exchange included in the range-separated HSE xc-functional via the parameter α in Figure 12. On the one

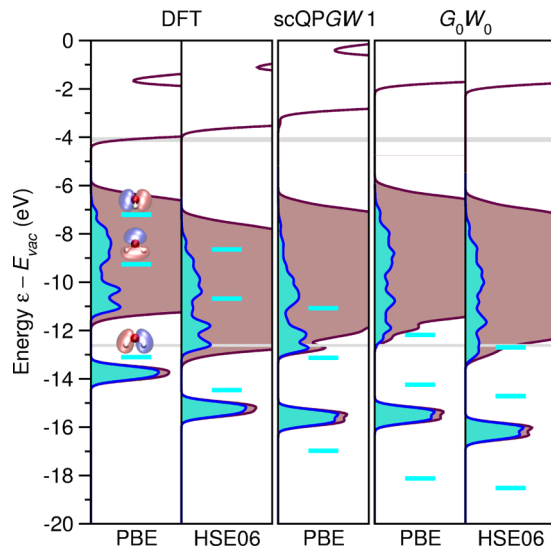


Figure 11. Absolute level alignment for 1ML intact H_2O adsorbed with antiparallel (\rightleftharpoons) interfacial hydrogen bonds on coordinately unsaturated Ti sites ($\text{H}_2\text{O}@\text{Ti}_{\text{cus}}$). Total (maroon) and H_2O projected (blue) DOS computed with DFT, scQPGW1, and $G_0\text{W}_0$ using the generalized gradient approximation (PBE) and hybrid (HSE) xc-functionals. Energies are relative to the vacuum level E_{vac} . The measured ϵ_{CBM} from ref 40 (thick gray line), measured and coupled-cluster (CCSD(T)) H_2O gas phase ionization potentials IP from ref 80 (thin gray line), and for each level of theory the calculated gas phase 1b_1 , 3a_1 , and 1b_2 H_2O levels (marked in cyan) are provided.

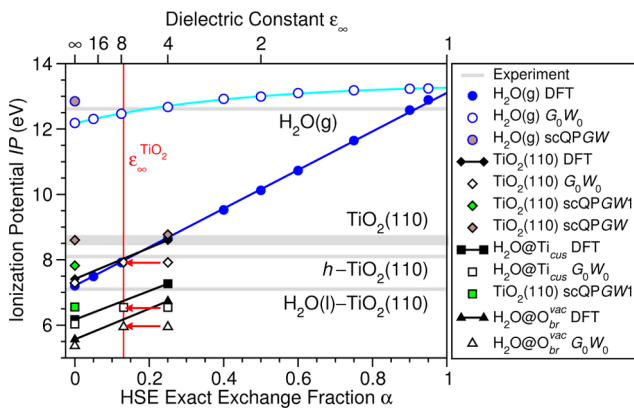


Figure 12. Ionization potential IP versus exact exchange fraction α included in the HSE xc-functional and equivalent dielectric constant $\epsilon_{\infty} \approx \alpha^{-1}$ from DFT (filled symbols), $G_0\text{W}_0$ (open symbols), scQPGW1 (green filled symbols), and scQPGW (brown filled symbols) for H_2O in gas phase (circles), a clean²³ (diamonds) and a $1^{1/2}\text{ML}$ of intact $\text{H}_2\text{O}@\text{Ti}_{\text{cus}}$ (squares) on the stoichiometric $\text{TiO}_2(110)$ surface, and a $1^{1/2}\text{ML}$ of dissociated $\text{H}_2\text{O}@O_{\text{br}}^{\text{vac}}$ (triangles) on the defective $\text{TiO}_{2-1/4}(110)$ surface with $1/2\text{ML}$ of $O_{\text{br}}^{\text{vac}}$. The measured IP for H_2O in gas phase,⁸⁰ the stoichiometric $\text{TiO}_2(110)$ surface,^{23,81–84} the 6–9% hydroxylated $h\text{-TiO}_2(110)$ surface,⁸³ and the liquid $\text{H}_2\text{O}-\text{TiO}_2(110)$ interface⁴⁰ are shown in gray. The self-consistent QP GW IP for H_2O in gas phase is indicated by the horizontal dashed line. The experimental dielectric constant of bulk TiO_2 , $\epsilon_{\infty}^{\text{TiO}_2} \approx 7.6$,⁸⁵ averaged over the (110) surface is marked in red. A linear fit to the DFT IP (blue), and an exponential fit to the $G_0\text{W}_0$ IP (cyan) for H_2O in gas phase are provided for comparison.

hand, for DFT, we find a strong linear dependence of IP on α , i.e., $IP \approx IP_{\text{PBE}} + (IP_{\alpha=1} - IP_{\text{PBE}})\alpha \approx 7.2 + 5.9\alpha$, with $\alpha \sim 0.9$ providing a quantitative agreement with experiment and

CCD(T) calculations. Overall, this linear dependence is not surprising, as α may be interpreted as the amount of electron–electron screening, i.e., the inverse dielectric constant ϵ_{∞}^{-1} .^{90,91} In other words, the fraction of exact exchange α included determines the amount of screening, ϵ_{∞}^{-1} , incorporated within the xc-functional. The quantitative agreement of the IP for $\alpha \sim 0.9$ is because small molecules, e.g., H_2O , are weakly screened in the gas phase ($\epsilon_{\infty} \sim 1$).

On the other hand, for $G_0\text{W}_0$, the calculated IP has a much weaker dependence on α , i.e., the starting xc-functional, with $IP \approx IP_{\alpha=1} - \Delta IP(10^{\alpha-1} - 1) \approx 13.4 - 1.2 \times 10^{-\alpha}$. Further, the $G_0\text{W}_0$ and DFT IP coincide when $\alpha \rightarrow 1$. For $G_0\text{W}_0$ based on PBE ($\alpha = 0$), the IP already agrees semiquantitatively with experiment, with full quantitative agreement obtained for $G_0\text{W}_0$ based on HSE06 ($\alpha = 0.25$). This is because the RPA $\epsilon_{\infty} \sim 1$, independently of α . Essentially, the calculated $G_0\text{W}_0$ IP s would also be obtained from DFT using an HSE xc-functional with $0.84 < \alpha < 1.0$, i.e., $1 < \epsilon_{\infty} < 1.2$. Overall, this implies $G_0\text{W}_0$ is a predictive method for the IP of small molecules. However, the scQPGW technique has the added advantage of being completely independent of the starting xc-functional,^{23,88} while providing a nearly quantitative IP .

For the $\text{H}_2\text{O}-\text{TiO}_2(110)$ interface, e.g., 1ML intact $\text{H}_2\text{O}@\text{Ti}_{\text{cus}}$, the highest energy H_2O PDOS peak, $\epsilon_{\text{peak}}^{\text{PDOS}}$, is pinned ~ 1 eV below the VBM across PBE DFT, HSE DFT, PBE scGW1, PBE $G_0\text{W}_0$, and HSE $G_0\text{W}_0$. For this reason, the IP of the H_2O interfacial levels is controlled by the alignment of the VBM with respect to the vacuum. This means we only need to consider the absolute VBM level alignment of the interface, i.e., the interface's $IP = -E_{\text{VBM}} + E_{\text{vac}}$ as a descriptor of photoelectrocatalytic activity.

In Figure 11 we see that the IP of the interface follows a different ordering across the methodologies from that of gas phase H_2O . In particular, we find PBE $G_0\text{W}_0$ (6.0 eV) \sim PBE DFT $<$ HSE06 $G_0\text{W}_0 \approx$ PBE scQPGW1 $<$ HSE06 DFT (7.3 eV). Figure 12 shows that, as was the case for H_2O in gas phase, the IP of the $\text{H}_2\text{O}@\text{Ti}_{\text{cus}}$ interface across the various methods is ordered according to the method's description of the screening, ϵ_{∞}^{-1} .

As discussed above, for hybrid xc-functionals such as HSE, the effective screening is determined by the fraction of exact exchange α included. Essentially, α plays the role of the effective screening within the method, ϵ_{∞}^{-1} . Although HSE06 incorporates less screening ($\epsilon_{\infty} \approx 4$) than experiment for rutile TiO_2 ($\epsilon_{\infty}^{\text{TiO}_2} \approx 7.6$),⁸⁵ the HSE06 IP for the interface is in agreement with the experimental estimate of $IP \approx 7.1$ eV.^{40,86}

If one performs $G_0\text{W}_0$ based on HSE06, a stronger screening is applied, i.e., $\epsilon_{\infty} \approx 5.7$, yielding a lower IP for the interface. In fact, as indicated by the red arrow in Figure 12, a similar IP to HSE06 $G_0\text{W}_0$ should be obtained from HSE DFT by setting the fraction of exact exchange to the inverse dielectric constant of bulk TiO_2 , i.e., $\alpha = 1/\epsilon_{\infty}^{\text{TiO}_2}$. Adjusting α to the measured inverse dielectric constant has been previously found to give improved band gaps.⁹⁰ From PBE scQPGW1, one obtains an IP consistent with that of HSE06 $G_0\text{W}_0$. This is because we find the screening in scQPGW decreases from PBE RPA with each self-consistent cycle. Essentially, the final screening incorporated in scQPGW1 is similar to that of HSE06 RPA.

As shown in Figure 11, PBE $G_0\text{W}_0$ gives an IP slightly lower than PBE DFT for the interface, while the PBE $G_0\text{W}_0$ CBM is shifted up by about 2 eV. This is surprising, since PBE DFT already yields a CBM level alignment for the interface in excellent agreement with experiment. This is partially due to

PBE RPA's overestimation of the screening of TiO_2 ($\epsilon_{\infty} \sim 8.3$). Although HSE06 G_0W_0 has a weaker screening than PBE G_0W_0 , the resulting absolute alignment of the CBM is quite similar. If instead, the self-energy corrections are applied self-consistently via PBE scQPGW1, the absolute alignment of the CBM is significantly lower but still greater than that of PBE DFT or HSE06 DFT. This is again related to decreases in the dielectric constant with each self-consistent cycle. For this reason, scQPGW1 tends to provide reasonable band gaps for $\text{TiO}_2(110)$ interfaces. Overall, we observe an ordering in increasing band gap of PBE DFT < HSE06 DFT \lesssim PBE scQPGW1 < PBE $G_0W_0 \approx$ HSE06 G_0W_0 , with HSE06 DFT providing the best absolute alignment of the CBM and VBM for the $\text{H}_2\text{O}@\text{Ti}_{\text{cav}}$ interface.

In Figure 12, we show that a similar correlation between IP and the method's description of screening holds for clean and hydroxylated $h\text{-TiO}_2(110)$. Specifically, we consider clean stoichiometric $\text{TiO}_2(110)$ ²³ and dissociated $\text{H}_2\text{O}@\text{O}_{\text{br}}^{\text{vac}}$ on defective $\text{TiO}_{2-1/4}(110)$ with $1/2\text{ML}$ of $\text{O}_{\text{br}}^{\text{vac}}$. Overall, $IP \approx IP_{\text{PBE}} + 5.9\alpha$ for all systems considered. We again find that the IP of PBE $G_0W_0 \sim$ PBE DFT, HSE06 $G_0W_0 \sim$ HSE($\alpha^{-1} = \epsilon_{\infty}^{\text{TiO}_2}$) \sim PBE scGW1, and PBE scQPGW \approx HSE06 scQPGW \sim HSE06 DFT.

HSE06 DFT provides the most accurate description of the IP of the clean and $\text{H}_2\text{O}@\text{Ti}_{\text{cav}}$ covered stoichiometric $\text{TiO}_2(110)$ surfaces. Although the HSE06 DFT IP for $\text{H}_2\text{O}@\text{O}_{\text{br}}^{\text{vac}}$ is significantly lower than the one measured for $h\text{-TiO}_2(110)$, in both cases, the IP is shifted to lower energies relative to the clean stoichiometric surface. Differences in the magnitude of the shifts are probably due to the differences in defect coverage between the experiment (6–9%)⁸³ and the calculation (50%).

The similarity between HSE06 DFT and scQPGW based on either PBE or HSE06 for the clean $\text{TiO}_2(110)$ surface²³ points to a similar screening from these two techniques. This also demonstrates the starting point independence of the scQPGW technique.

To summarize, although scQPGW provides accurate IP s, the band gap is greatly overestimated, as reported previously.^{22,23,41,92} While scQPGW1 provides a more accurate band gap, it achieves only a qualitative description of the IP . HSE06 achieves a quantitative description of both the IP and band gap but provides a poor description of the molecular level alignment relative to the VBM.^{22,23,92} However, since the highest occupied H_2O levels are significantly hybridized with the substrate, this is not a major drawback in this case. In general, for $\text{TiO}_2(110)$, a more effective strategy is to combine the calculated IP from HSE06 with the occupied interfacial levels' alignment from G_0W_0 or scQPGW1.

4. CONCLUSIONS

The level alignment prior to photoirradiation is an important piece of the puzzle needed to get a complete atomistic picture of photocatalytic processes. Here we have shown that the complex UPS spectra for the $\text{H}_2\text{O}-\text{TiO}_2$ interface may be disentangled using QP G_0W_0 PDOS. We have firmly established the robustness of the QP G_0W_0 H_2O PDOS by (1) demonstrating its xc-functional (PBE, LDA, vdW-DF, and HSE06) independence, (2) comparing to self-consistent QP GW techniques (scQPGW1), and (3) considering its dependence on surface coverage and dissociation. Altogether, these calculations provide an accurate interpretation of the complex UPS and MIES experiments^{18,25,26} for the $\text{H}_2\text{O}-\text{TiO}_2(110)$

interface and provide accurate estimates of the highest H_2O occupied levels' alignment relative to the VBM.

Our results provide two important pieces of the puzzle: (1) the molecular structure of the photocatalytic interface and (2) the molecular alignment of the doubly occupied levels near the VBM responsible for hole trapping prior to irradiation. To complete the picture, the molecular structure and level alignment in the presence of the photogenerated hole is also needed. Previous DFT studies using the hybrid HSE xc-functional have found a hole can be trapped at surface O $2p_{\pi}$ levels of O_{br} and $\text{HO}-\text{Ti}_{\text{cav}}$ sites.⁵ However, the screening of such localized levels may not be well described by HSE, which tends to underbind localized interfacial levels.²³ This underbinding is corrected upon inclusion of many-body effects via QP G_0W_0 .²³ Having demonstrated the capability of G_0W_0 for the description of level alignment prior to irradiation, this work points the way forward via future QP G_0W_0 studies of level alignment for trapped hole levels.

■ ASSOCIATED CONTENT

Supporting Information

Total energies and optimized geometries. This material is available free of charge via the Internet at <http://pubs.acs.org>.

■ AUTHOR INFORMATION

Corresponding Author

*E-mail: annapaola.migani@cin2.es.

Notes

The authors declare no competing financial interest.

■ ACKNOWLEDGMENTS

We acknowledge fruitful discussions with Angel Rubio, and we thank Stefan Krischok for providing experimental data. We acknowledge funding from Spanish Grants (FIS2012-37549-C05-02, RYC-2011-09582, JCI-2010-08156); Generalitat de Catalunya (2014SGR301, XRQTC); Grupos Consolidados UPV/EHU del Gobierno Vasco (IT-578-13); NSFC (21003113 and 21121003); MOST (2011CB921404); and NSF Grant CHE-1213189; and computational time from BSC Red Espanola de Supercomputacion and EMSL at PNNL by the DOE.

■ REFERENCES

- (1) Thompson, T. L.; Yates, J. T. J. Surface Science Studies of the Photoactivation of TiO_2 —New Photochemical Processes. *Chem. Rev.* **2006**, *106*, 4428–4453.
- (2) Henderson, M. A. A surface science perspective on TiO_2 photocatalysis. *Surf. Sci. Rep.* **2011**, *66*, 185–297.
- (3) Tan, S.; Feng, H.; Ji, Y.; Wang, Y.; Zhao, J.; Zhao, A.; Wang, B.; Luo, Y.; Yang, J.; Hou, J. G. Observation of Photocatalytic Dissociation of Water on Terminal Ti Sites of $\text{TiO}_2(110)-1 \times 1$ Surface. *J. Am. Chem. Soc.* **2012**, *134*, 9978–9985.
- (4) Cheng, J.; Sulpizi, M.; VandeVondele, J.; Sprik, M. Hole Localization and Thermochemistry of Oxidative Dehydrogenation of Aqueous Rutile $\text{TiO}_2(110)$. *ChemCatChem* **2012**, *4*, 636–640.
- (5) Cheng, J.; VandeVondele, J.; Sprik, M. Identifying Trapped Electronic Holes at the Aqueous TiO_2 Interface. *J. Phys. Chem. C* **2014**, *118*, 5437–5444.
- (6) Nakamura, R.; Nakato, Y. Primary Intermediates of Oxygen Photoevolution Reaction on TiO_2 (Rutile) Particles, Revealed by in Situ FTIR Absorption and Photoluminescence Measurements. *J. Am. Chem. Soc.* **2004**, *126*, 1290–1298.
- (7) Imanishi, A.; Okamura, T.; Ohashi, N.; Nakamura, R.; Nakato, Y. Mechanism of Water Photooxidation Reaction at Atomically Flat TiO_2

- (Rutile) (110) and (100) Surfaces: Dependence on Solution pH. *J. Am. Chem. Soc.* **2007**, *129*, 11569–11578.
- (8) Waegele, M. M.; Chen, X.; Herlihy, D. M.; Cuk, T. How Surface Potential Determines the Kinetics of the First Hole Transfer of Photocatalytic Water Oxidation. *J. Am. Chem. Soc.* **2014**, *136*, 10632–10639.
- (9) Cheng, J.; Liu, X.; Kattirtzi, J. A.; VandeVondele, J.; Sprik, M. Aligning Electronic and Protonic Energy Levels of Proton-Coupled Electron Transfer in Water Oxidation on Aqueous TiO₂. *Angew. Chem., Int. Ed.* **2014**, *53*, 12046–12050.
- (10) Tritsaris, G. A.; Vinichenko, D.; Kolesov, G.; Friend, C. M.; Kaxiras, E. Dynamics of the Photogenerated Hole at the Rutile TiO₂(110)/Water Interface: A Nonadiabatic Simulation Study. *J. Phys. Chem. C* **2014**, DOI: <http://dx.doi.org/10.1021/jp508557w>.
- (11) Whitesides, G. M.; Crabtree, G. W. Don't Forget Long-Term Fundamental Research in Energy. *Science* **2007**, *315*, 796–798.
- (12) *The Energy Challenges Report: New Science for a Secure and Sustainable Energy Future*; Hemminger, J., Crabtree, G., Kastner, M., Eds.; Argonne National Laboratory: Argonne, IL, 2008.
- (13) Fujishima, A.; Honda, K. Electrochemical Photolysis of Water at a Semiconductor Electrode. *Nature* **1972**, *238*, 37–38.
- (14) Fujishima, A.; Zhang, X.; Tryk, D. A. TiO₂ photocatalysis and related surface phenomena. *Surf. Sci. Rep.* **2008**, *63*, 515–582.
- (15) Salvador, P. On the Nature of Photogenerated Radical Species Active in the Oxidative Degradation of Dissolved Pollutants with TiO₂ Aqueous Suspensions: A Revision in the Light of the Electronic Structure of Adsorbed Water. *J. Phys. Chem. C* **2007**, *111*, 17038–17043.
- (16) Salvador, P. Mechanisms of water photooxidation at *n*-TiO₂ rutile single crystal oriented electrodes under UV illumination in competition with photocorrosion. *Prog. Surf. Sci.* **2011**, *86*, 41–58.
- (17) Theoretical Insights into Photoinduced Charge Transfer and Catalysis at Oxide Interfaces. *Chem. Rev.* **2013**, *113*, 4496–4565.
- (18) Kurtz, R. L.; Stock-Bauer, R.; Madey, T. E.; Román, E.; Segovia, J. L. D. Synchrotron radiation studies of H₂O adsorption on TiO₂(110). *Surf. Sci.* **1989**, *218*, 178–200.
- (19) Neaton, J. B.; Hybertsen, M. S.; Louie, S. G. Renormalization of Molecular Electronic Levels at Metal-Molecule Interfaces. *Phys. Rev. Lett.* **2006**, *97*, 216405.
- (20) Garcia-Lastra, J. M.; Rostgaard, C.; Rubio, A.; Thygesen, K. S. Polarization-induced renormalization of molecular levels at metallic and semiconducting surfaces. *Phys. Rev. B* **2009**, *80*, 245427.
- (21) Patrick, C. E.; Giustino, F. Quantitative Analysis of Valence Photoemission Spectra and Quasiparticle Excitations at Chromophore-Semiconductor Interfaces. *Phys. Rev. Lett.* **2012**, *109*, 116801.
- (22) Migani, A.; Mowbray, D. J.; Iacomino, A.; Zhao, J.; Petek, H.; Rubio, A. Level Alignment of a Prototypical Photocatalytic System: Methanol on TiO₂(110). *J. Am. Chem. Soc.* **2013**, *135*, 11429–11432.
- (23) Migani, A.; Mowbray, D. J.; Zhao, J.; Petek, H.; Rubio, A. Quasiparticle level alignment for photocatalytic interfaces. *J. Chem. Theory Comput.* **2014**, *10*, 2103–2114.
- (24) Migani, A.; Mowbray, D. J. Coverage dependence of the level alignment for methanol on TiO₂(110). *Comput. Theor. Chem.* **2014**, *1040–1041*, 259–265.
- (25) Brookes, I. M.; Muryn, C. A.; Thornton, G. Imaging Water Dissociation on TiO₂(110). *Phys. Rev. Lett.* **2001**, *87*, 266103.
- (26) Krischok, S.; Höfft, O.; Günster, J.; Stultz, J.; Goodman, D.; Kempter, V. H₂O interaction with bare and Li-precovered TiO₂: studies with electron spectroscopies (MIES and UPS(HeI and II)). *Surf. Sci.* **2001**, *495*, 8–18.
- (27) Henderson, M. A. An HREELS and TPD study of water on TiO₂(110): the extent of molecular versus dissociative adsorption. *Surf. Sci.* **1996**, *355*, 151–166.
- (28) Lindan, P. J. D.; Harrison, N. M.; Gillan, M. J. Mixed Dissociative and Molecular Adsorption of Water on the Rutile (110) Surface. *Phys. Rev. Lett.* **1998**, *80*, 762–765.
- (29) Schaub, R.; Thostrup, P.; Lopez, N.; Lægsgaard, E.; Stensgaard, I.; Nørskov, J. K.; Besenbacher, F. Oxygen Vacancies as Active Sites for Water Dissociation on Rutile TiO₂(110). *Phys. Rev. Lett.* **2001**, *87*, 266104.
- (30) Harris, L. A.; Quong, A. A. Molecular Chemisorption as the Theoretically Preferred Pathway for Water Adsorption on Ideal Rutile TiO₂(110). *Phys. Rev. Lett.* **2004**, *93*, 086105.
- (31) Lindan, P. J. D.; Zhang, C. Exothermic water dissociation on the rutile TiO₂(110) surface. *Phys. Rev. B* **2005**, *72*, 075439.
- (32) Liu, L.-M.; Zhang, C.; Thornton, G.; Michaelides, A. Structure and dynamics of liquid water on rutile TiO₂(110). *Phys. Rev. B* **2010**, *82*, 161415.
- (33) Amft, M.; Walle, L. E.; Ragazzon, D.; Borg, A.; Uvdal, P.; Skorodumova, N. V.; Sandell, A. A Molecular Mechanism for the Water–Hydroxyl Balance during Wetting of TiO₂. *J. Phys. Chem. C* **2013**, *117*, 17078–17083.
- (34) Walle, L. E.; Ragazzon, D.; Borg, A.; Uvdal, P.; Sandell, A. Photoemission studies of water dissociation on rutile TiO₂: Aspects on experimental procedures and the influence of steps. *Appl. Surf. Sci.* **2014**, *303*, 245–249.
- (35) Walle, L.; Ragazzon, D.; Borg, A.; Uvdal, P.; Sandell, A. Competing water dissociation channels on rutile TiO₂(110). *Surf. Sci.* **2014**, *621*, 77–81.
- (36) Du, Y.; Deskins, N. A.; Zhang, Z.; Dohnálek, Z.; Dupuis, M.; Lyubinetsky, I. Two Pathways for Water Interaction with Oxygen Adatoms on TiO₂(110). *Phys. Rev. Lett.* **2009**, *102*, 096102.
- (37) Turner, D. W.; Baker, C.; Baker, A. D.; Brundle, C. R. *Molecular Photoelectron Spectroscopy*; Wiley-Interscience: New York, 1970; p 113.
- (38) Connor, J.; Considine, M.; Hillier, I.; Briggs, D. Low energy photoelectron spectroscopy of solids. Aspects of experimental methodology concerning metals and insulators. *J. Electron Spectrosc. Relat. Phenom.* **1977**, *12*, 143–159.
- (39) Cheng, J.; Sprik, M. Alignment of electronic energy levels at electrochemical interfaces. *Phys. Chem. Chem. Phys.* **2012**, *14*, 11245–11267.
- (40) Cheng, J.; Sprik, M. Aligning electronic energy levels at the TiO₂/H₂O interface. *Phys. Rev. B* **2010**, *82*, 081406.
- (41) Shishkin, M.; Marsman, M.; Kresse, G. Accurate Quasiparticle Spectra from Self-Consistent GW Calculations with Vertex Corrections. *Phys. Rev. Lett.* **2007**, *99*, 246403.
- (42) van Schilfgaarde, M.; Kotani, T.; Faleev, S. Quasiparticle Self-Consistent GW Theory. *Phys. Rev. Lett.* **2006**, *96*, 226402.
- (43) Kotani, T.; van Schilfgaarde, M.; Faleev, S. V.; Chantis, A. Quasiparticle self-consistent GW method: a short summary. *J. Phys.: Condens. Matter* **2007**, *19*, 365236.
- (44) Hedin, L. New Method for Calculating the One-Particle Green's Function with Application to the Electron-Gas Problem. *Phys. Rev.* **1965**, *139*, A796–A823.
- (45) Onida, G.; Reining, L.; Rubio, A. Electronic excitations: densityfunctional versus many-body Green's-function approaches. *Rev. Mod. Phys.* **2002**, *74*, 601–659.
- (46) Shishkin, M.; Kresse, G. Implementation and performance of the frequency-dependent GW method within the PAW framework. *Phys. Rev. B* **2006**, *74*, 035101.
- (47) Kresse, G.; Joubert, D. From ultrasoft pseudopotentials to the projector augmented-wave method. *Phys. Rev. B* **1999**, *59*, 1758.
- (48) Perdew, J. P.; Burke, K.; Ernzerhof, M. Generalized Gradient Approximation Made Simple. *Phys. Rev. Lett.* **1996**, *77*, 3865.
- (49) Kresse, G.; Furthmüller, J. Efficient iterative schemes for ab initio totalenergy calculations using a plane-wave basis set. *Phys. Rev. B* **1996**, *54*, 11169.
- (50) Perdew, J. P.; Zunger, A. Self-interaction correction to density-functional approximations for many-electron systems. *Phys. Rev. B* **1981**, *23*, 5048–5079.
- (51) Dion, M.; Rydberg, H.; Schröder, E.; Langreth, D. C.; Lundqvist, B. I. Van der Waals Density Functional for General Geometries. *Phys. Rev. Lett.* **2004**, *92*, 246401.
- (52) Heyd, J.; Scuseria, G. E.; Ernzerhof, M. Hybrid functionals based on a screened Coulomb potential. *J. Chem. Phys.* **2003**, *118*, 8207.

- (53) Kruckau, A. V.; Vydrov, O. A.; Izmaylov, A. F.; Scuseria, G. E. Influence of the exchange screening parameter on the performance of screened hybrid functionals. *J. Chem. Phys.* **2006**, *125*, 224106.
- (54) Burdett, J. K.; Hugbanks, T.; Miller, G. J.; Richardson, J. W.; Smith, J. V. Structural-electronic relationships in inorganic solids: powder neutron diffraction studies of the rutile and anatase polymorphs of titanium dioxide at 15 and 295 K. *J. Am. Chem. Soc.* **1987**, *109*, 3639–3646.
- (55) Despoja, V.; Lončarić, I.; Mowbray, D. J.; Marušić, L. Quasiparticle spectra and excitons of organic molecules deposited on substrates: G_0W_0 -BSE approach applied to benzene on graphene and metallic substrates. *Phys. Rev. B* **2013**, *88*, 235437.
- (56) Despoja, V.; Mowbray, D. J. Using surface plasmonics to turn on fullerene's dark excitons. *Phys. Rev. B* **2014**, *89*, 195433.
- (57) Hammer, B.; Hansen, L. B.; Nørskov, J. K. Improved Adsorption Energetics within Density-Functional Theory Using Revised Perdew-Burke-Ernzerhof Functionals. *Phys. Rev. B* **1999**, *59*, 7413–7421.
- (58) Lee, J.; Sorescu, D. C.; Deng, X.; Jordan, K. D. Water Chain Formation on $\text{TiO}_2(110)$. *J. Phys. Chem. Lett.* **2013**, *4*, 53–57.
- (59) Kimmel, G. A.; Baer, M.; Petrik, N. G.; VandeVondele, J.; Rousseau, R.; Mundy, C. J. Polarization- and Azimuth-Resolved Infrared Spectroscopy of Water on $\text{TiO}_2(110)$: Anisotropy and the Hydrogen-Bonding Network. *J. Phys. Chem. Lett.* **2012**, *3*, 778–784.
- (60) Shapovalov, V.; Wang, Y.; Truong, T. N. Theoretical analysis of the electronic spectra of water adsorbed on the rutile $\text{TiO}_2(110)$ and $\text{MgO}(100)$ surfaces. *Chem. Phys. Lett.* **2003**, *375*, 321–327.
- (61) Mowbray, D. J.; Martínez, J. I.; Calle-Vallejo, F.; Rossmeisl, J.; Thygesen, K. S.; Jacobsen, K. W.; Nørskov, J. K. Trends in Metal Oxide Stability for Nanorods, Nanotubes, and Surfaces. *J. Phys. Chem. C* **2011**, *115*, 2244–2252.
- (62) Lun Pang, C.; Lindsay, R.; Thornton, G. Chemical reactions on rutile $\text{TiO}_2(110)$. *Chem. Soc. Rev.* **2008**, *37*, 2328–2353.
- (63) Minato, T.; Sainoo, Y.; Kim, Y.; Kato, H. S.; Aika, K.-i.; Kawai, M.; Zhao, J.; Petek, H.; Huang, T.; He, W.; et al. The electronic structure of oxygen atom vacancy and hydroxyl impurity defects on titanium dioxide (110) surface. *J. Chem. Phys.* **2009**, *130*, 124502.
- (64) Di Valentin, C.; Pacchioni, G.; Selloni, A. Electronic Structure of Defect States in Hydroxylated and Reduced Rutile $\text{TiO}_2(110)$ Surfaces. *Phys. Rev. Lett.* **2006**, *97*, 166803.
- (65) Allegretti, F.; O'Brien, S.; Polcik, M.; Sayago, D. I.; Woodruff, D. P. Adsorption Bond Length for H_2O on $\text{TiO}_2(110)$: A Key Parameter for Theoretical Understanding. *Phys. Rev. Lett.* **2005**, *95*, 226104.
- (66) Allegretti, F.; O'Brien, S.; Polcik, M.; Sayago, D.; Woodruff, D. Quantitative determination of the local structure of H_2O on $\text{TiO}_2(100)$ using scanned-energy mode photoelectron diffraction. *Surf. Sci. Sci.* **2006**, *600*, 1487–1496.
- (67) Papageorgiou, A. C.; Beglitis, N. S.; Pang, C. L.; Teobaldi, G.; Cabailh, G.; Chen, Q.; Fisher, A. J.; Hofer, W. A.; Thornton, G. Electron traps and their effect on the surface chemistry of $\text{TiO}_2(110)$. *Proc. Natl. Acad. Sci. U. S. A.* **2010**, *107*, 2391–2396.
- (68) Sun, C.; Liu, L.-M.; Selloni, A.; Lu, G. Q. M.; Smith, S. C. Titania-water interactions: a review of theoretical studies. *J. Mater. Chem.* **2010**, *20*, 10319–10334.
- (69) Zhao, J.; Li, B.; Jordan, K. D.; Yang, J.; Petek, H. Interplay between hydrogen bonding and electron solvation on hydrated $\text{TiO}_2(110)$. *Phys. Rev. B* **2006**, *73*, 195309.
- (70) Wu, Z.; Zhang, W.; Xiong, F.; Yuan, Q.; Jin, Y.; Yang, J.; Huang, W. Active hydrogen species on TiO_2 for photocatalytic H_2 production. *Phys. Chem. Chem. Phys.* **2014**, *16*, 7051–7057.
- (71) Kowalski, P. M.; Meyer, B.; Marx, D. Composition, structure, and stability of the rutile $\text{TiO}_2(110)$ surface: Oxygen depletion, hydroxylation, hydrogen migration, and water adsorption. *Phys. Rev. B* **2009**, *79*, 115410.
- (72) Zhang, C.; Lindan, P. J. D. Multilayer water adsorption on rutile $\text{TiO}_2(110)$: A first-principles study. *J. Chem. Phys.* **2003**, *118*, 4620–4630.
- (73) Garbuio, V.; Cascella, M.; Pulci, O. Excited state properties of liquid water. *J. Phys.: Condens. Matter* **2009**, *21*, 033101.
- (74) Montoya, J. F.; Ivanova, I.; Dillert, R.; Bahnemann, D. W.; Salvador, P.; Peral, J. Catalytic Role of Surface Oxygens in TiO_2 Photooxidation Reactions: Aqueous Benzene Photooxidation with Ti^{18}O_2 under Anaerobic Conditions. *J. Phys. Chem. Lett.* **2013**, *4*, 1415–1422.
- (75) Hoffmann, M. R.; Martin, S. T.; Choi, W.; Bahnemann, D. W. Environmental Applications of Semiconductor Photocatalysis. *Chem. Rev.* **1995**, *95*, 69–96.
- (76) Muryn, C.; Hardman, P.; Crouch, J.; Raiker, G.; Thornton, G.; Law, D. Step and point defect effects on $\text{TiO}_2(100)$ reactivity. *Surf. Sci.* **1991**, *251–252*, 747–752.
- (77) Tezuka, Y.; Shin, S.; Ishii, T.; Ejima, T.; Suzuki, S.; Sato, S. Photoemission and Bremsstrahlung Isochromat Spectroscopy Studies of TiO_2 (Rutile) and SrTiO_3 . *J. Phys. Soc. Jpn.* **1994**, *63*, 347–357.
- (78) Valentini, C. D.; Fittipaldi, D. Hole Scavenging by Organic Adsorbates on the TiO_2 Surface: A DFTModel Study. *J. Phys. Chem. Lett.* **2013**, *4*, 1901–1906.
- (79) Chen, J.; Li, Y.-F.; Sit, P.; Selloni, A. Chemical Dynamics of the First Proton-Coupled Electron Transfer of Water Oxidation on TiO_2 Anatase. *J. Am. Chem. Soc.* **2013**, *135*, 18774–18777.
- (80) Bruneval, F.; Marques, M. A. L. Benchmarking the Starting Points of the GW Approximation for Molecules. *J. Chem. Theory Comput.* **2013**, *9*, 324–329.
- (81) Chung, Y. W.; Lo, W. J.; Somorjai, G. A. Low energy electron diffraction and electron spectroscopy studies of the clean (110) and (100) titanium dioxide (rutile) crystal surfaces. *Surf. Sci.* **1977**, *64*, 588.
- (82) Onishi, H.; Aruga, T.; Egawa, C.; Iwasawa, Y. Adsorption of CH_3OH , HCOOH and SO_2 on $\text{TiO}_2(110)$ and stepped $\text{TiO}_2(441)$ surfaces. *Surf. Sci.* **1988**, *193*, 33–46.
- (83) Borodin, A.; Reichling, M. Characterizing $\text{TiO}_2(110)$ surface states by their work function. *Phys. Chem. Chem. Phys.* **2011**, *13*, 15442–15447.
- (84) Onda, K.; Li, B.; Petek, H. Two-photon photoemission spectroscopy of $\text{TiO}_2(110)$ surfaces modified by defects and O_2 or H_2O adsorbates. *Phys. Rev. B* **2004**, *70*, 045415.
- (85) Traylor, J. G.; Smith, H. G.; Nicklow, R. M.; Wilkinson, M. K. Lattice Dynamics of Rutile. *Phys. Rev. B* **1971**, *3*, 3457–3472.
- (86) Photoelectrochemical cells. *Nature* **2001**, *414*, 338–344.
- (87) Rostgaard, C.; Jacobsen, K. W.; Thygesen, K. S. Fully self-consistent GW calculations for molecules. *Phys. Rev. B* **2010**, *81*, 085103.
- (88) Caruso, F.; Rinke, P.; Ren, X.; Scheffler, M.; Rubio, A. Unified description of ground and excited states of finite systems: The self-consistent GW approach. *Phys. Rev. B* **2012**, *86*, 081102.
- (89) van Setten, M. J.; Weigend, F.; Evers, F. The GW-Method for Quantum Chemistry Applications: Theory and Implementation. *J. Chem. Theory Comput.* **2013**, *9*, 232–246.
- (90) Marques, M. A. L.; Vidal, J.; Oliveira, M. J. T.; Reining, L.; Botti, S. Density-based mixing parameter for hybrid functionals. *Phys. Rev. B* **2011**, *83*, 035119.
- (91) Skone, J. H.; Govoni, M.; Galli, G. Self-consistent hybrid functional for condensed systems. *Phys. Rev. B* **2014**, *89*, 195112.
- (92) Pacchioni, G. First Principles Calculations on Oxide-Based Heterogeneous Catalysts and Photocatalysts: Problems and Advances. *Catal. Lett.* **2014**, 1–15.